FACULDADE DE ENGENHARIA DA UNIVERSIDADE DO PORTO

A low-Mach number solver for closed systems with real-fluid thermodynamics

Gonçalo de Vasco Mendes e Pereira Alcobia

THIS THESIS WAS DEVELOPED AT THE DELFT UNIVERSITY OF TECHNOLOGY AS PART OF THE ERASMUS+ PROGRAM AND SUBMITTED TO THE UNIVERSITY OF PORTO FOR THE DEGREE OF:

MSc in Mechanical Engineering - Fluids and Energies

Host University Supervisor: Pedro Simões Costa, TU Delft

Host University Supervisor: Rene Pecnik, TU Delft

Co-Supervisor: Sanath Kottursheltar, TU Delft

Home University Supervisor: Célio Bruno Pinto Fernandes, FEUP

July 29, 2025

Aos meus queridos Pais
Aos meus irmãos
À Duda

Abstract

In recent decades, the energy transition has brought increasing challenges in terms of optimising the efficiency of thermal systems and reducing their environmental impact. This challenge requires robust and generalised numerical models capable of accurately simulating heat transfer in complex regimes, often involving real fluids (with non-zero viscosity) under extreme pressure and temperature conditions. An alternative to the fully compressible Navier-Stokes equations, which are highly demanding from a computational point of view, is the low Mach number formulation, which filters out acoustic waves and allows for larger time steps while maintaining an accurate description of thermal convection. Although previous studies using direct numerical simulation (DNS) with the low Mach formulation have made a significant contribution to understanding the mechanisms of heat transfer and transport of properties in real fluids, there is still a significant gap in the modeling of closed systems (where mass is conserved over time) for real fluids. This thesis addresses this gap by introducing a generalised formulation of the low-Mach number equations for real fluids in closed systems, in which the governing equations are reformulated to ensure consistent closure of the thermodynamic system. The proposed approach guarantees global mass conservation and integrates an iterative Newton-Raphson method to update the thermodynamic pressure compatible with any equation of state (EoS). The CoolProp library was used to calculate the thermodynamic properties because of its wide range of fluids and high precision. The algorithm was validated in the ideal gas limit in a differentially heated cavity (DHC) with different vertical wall temperature ratios ($T_h/T_c = 1.5,\ 2,$ and 3). At these temperature differences, the thermodynamic properties undergo substantial changes to influence the flow dynamics. Simulations were then carried out with supercritical carbon dioxide (sCO_2) and pressurised liquid water at 20 MPa, at temperature ratios of $T_h/T_c = 1.5$ and 2, representing different thermodynamic scenarios. The results showed that the solver is capable of reproducing physically consistent trends in the temperature, velocity, and Nusselt number profiles, demonstrating its potential as a robust tool for heat transfer simulations with real fluids in the low Mach number regime.

Keywords: Direct numerical simulations, real fluid thermodynamics, low Mach number flows, closed systems, differentially heated cavity

Resumo

Nas últimas décadas, a transição energética tem vindo a colocar cada vez mais desafios no sentido de otimizar a eficiência dos sistemas térmicos e reduzir o seu impacto ambiental. Este desafio exige modelos numéricos robustos e generalizados, capazes de simular com precisão a transferência de calor em regimes complexos, muitas vezes envolvendo fluidos reais (com viscosidade não nula) em condições extremas de pressão e temperatura. Uma alternativa às equações de Navier-Stokes totalmente compressíveis, que são altamente exigentes do ponto de vista computacional, é a formulação de baixo número de Mach, que filtra as ondas acústicas e permite maiores passos de tempo, mantendo uma descrição precisa da convecção térmica. Embora estudos anteriores de simulação numérica direta (DNS) com esta formulação tenham contribuído significativamente para a compreensão dos mecanismos de transferência de calor e transporte de propriedades em fluidos reais, subsiste uma lacuna importante na modelação de sistemas fechados (sistemas nos quais a massa se conserva ao longo do tempo) para fluidos reais utilizando a formulação de baixo número de Mach. Com o objetivo de colmatar esta lacuna, o presente trabalho propõe uma formulação generalizada das equações de baixo número de Mach para fluidos reais em sistemas fechados, garantindo o fecho das equações do sistema termodinâmico através da sua reformulação. A abordagem proposta garante a conservação global de massa e integra um método iterativo de Newton–Raphson para atualizar a pressão termodinâmica compatível com qualquer equação de estado (EoS). A biblioteca *CoolProp* foi utilizada para o cálculo das propriedades termodinâmicas devido à sua ampla gama de fluidos e elevada precisão. O algoritmo foi validado no limite do gás ideal numa cavidade aquecida diferencialmente (DHC), com diferentes razões de temperatura nas paredes verticais ($T_h/T_c = 1.5,\ 2, \text{e } 3$). A estas diferenças de temperatura, as propriedades termodinâmicas sofrem alterações substanciais que influenciam a dinâmica do escoamento. Posteriormente, realizaram-se simulações com dióxido de carbono supercrítico (sCO_2) e água líquida pressurizada a 20 MPa, para razões de temperatura $T_h/T_c = 1.5$ e 2, representando cenários termodinâmicos distintos. Os resultados obtidos pelo algoritmo desenvolvido mostraram que o mesmo é capaz de reproduzir tendências fisicamente consistentes nos perfis de temperatura, velocidade e número de Nusselt, evidenciando o seu potencial como ferramenta robusta para simulações de transferência de calor com fluidos reais no regime de baixo número de Mach.

Palavras-chave: Simulações diretas de Navier-Stokes, termodinâmica de fluidos reais, escoamentos a baixo número de Mach, sistemas fechados, cavidade aquecida diferencialmente

Acknowledgements

This dissertation represents a long and beautiful journey filled with challenges, discoveries, and personal growth. Throughout this path, I was fortunate to count on the support of people who, in different ways, contributed to making this work and the entire academic journey that preceded it possible. May you find in these words my deepest thanks and sincere gratitude.

First and foremost, I would like to thank my supervisor at TU Delft, Professor Pedro Costa, for his scientific guidance, insightful discussions, and the trust he placed in me to carry out this work autonomously. I also express my gratitude to Professor Rene Pecnik from TU Delft for his critical insight and deep knowledge, which significantly enriched this work, and to Ph.D. student Sanath Kottursheettar for his tireless technical support, patience, and generosity in sharing his expertise throughout the entire process.

I would like to give a special thank you to Professor Célio Fernandes, co-supervisor of this work from FEUP, who has been an inspiration since my very first year of the Master's program. He was the one who encouraged me to pursue scientific research and with whom I had the opportunity to collaborate on several projects that greatly contributed to my academic and personal growth. Beyond his role as a researcher, Professor Célio has been a true mentor - always available, attentive, and offering the right words, even in the most demanding moments. His support, both scientific and emotional, has had a profound impact on this journey.

To my friends, I extend my heartfelt thanks - life simply wouldn't be the same without you. To those from Coimbra, who have been with me since childhood and continue to welcome me with the same warmth every time I return to the city where I grew up. To those I met during my undergraduate studies at FCUP, with whom I shared not only academic challenges but also meaningful moments that helped shape who I am. And to the friends I made at FEUP and in Porto, who became an essential part of this chapter. Each of you, in your own way, has been (and continues to be) a fundamental pillar in my life. Your friendship has been a constant refuge and a quiet but powerful force throughout this entire journey. I choose not to name you, not because you are many, but out of fear of being unfair. You know who you are, and I hope these words convey the special place you hold in my heart.

To Duda, my girlfriend, I owe a thank you that goes far beyond words. Thank you for walking this journey with me, with love, patience, and understanding at every moment. Your constant support and presence made this path lighter and far more beautiful.

Finally, I want to express my deepest gratitude to my parents, Maria João and Carlos, for the values they instilled in me, for their unconditional support, and for always being there through every stage of my life. With the same love and affection, I thank my siblings, Joana and Diogo, for their love, companionship, and the way that they have always been with me through both joyful and difficult times. The four of you have always been (and will always be) my safe harbor.

"Doubt is the origin of wisdom."

- René Descartes

Contents

List of Figures

List of Tables

Abbreviations and Symbols

Roman Symbols

a	Speed of sound $[m\ s^{-1}]$
e	Internal energy per unit mass $[J\ kg^{-1}]$
e_t	Total energy per unit mass $[J\ kg^{-1}]$
f	Force per unit mass $[m\ s^{-2}]$
f	Generic mathematical function
g	Gravitational acceleration $[m\ s^{-2}]$
$\vec{g}$	Gravitational acceleration vector $[m\ s^{-2}]$
h_s	Sensible enthalpy per unit mass $[J\ kg^{-1}]$
h_t	Total enthalpy per unit mass $[J\ kg^{-1}]$
k	Turbulent kinetic energy $[m^2\ s^{-2}]$
k	Substep of Runge–Kutta time integration
m_0	Total mass in closed system $[kg]$
n	Time step index
n_i	Unit normal vector component
n_{NR}	Newton-Raphson iteration index
p	Total pressure $[Pa]$
p_0	Thermodynamic pressure $[Pa]$
p_1	Hydrodynamic pressure $[Pa]$
q_i	Heat flux in i-th direction $[W\ m^{-2}]$
r	Richardson extrapolation order of convergence
s	Specific entropy $[J\ kg^{-1}\ K^{-1}]$
t	Time $[s]$
u	Horizontal velocity $[m\ s^{-1}]$
u_i	i-th component of velocity vector $[m\ s^{-1}]$
u_j	j-th component of velocity vector $[m\ s^{-1}]$
v	Transverse velocity $[m\ s^{-1}]$
w	Vertical velocity $[m\ s^{-1}]$
x	Horizontal spatial coordinate $[m]$
x_i	i-th Cartesian coordinate $[m]$

x_j	j-th Cartesian coordinate $[m]$
z	Vertical spatial coordinate $[m]$
C	Constant for Richarson extrapolation
C_p	Specific heat at constant pressure $[J\ kg^{-1}\ K^{-1}]$
C_v	Specific heat at constant volume $[J\ kg^{-1}\ K^{-1}]$
L	Characteristic length (cavity height) [m]
M	Mach number
Nu	Nusselt number
Pe	Péclet number
$\dot{Q}$	Heat transfer rate $[W]$
R	Numerical result used in Richardson extrapolation
Ra	Rayleigh number
Re	Reynolds number
R_{ext}	Extrapolated value of Richardson extrapolation
R_i	Result R computed on the i-th mesh
S	Surface area $[m^2]$
T	Temperature $[K]$
V	Volume $[m^3]$

Greek Symbols

α	Thermal diffusivity $[m^2\ s^{-1}]$
α^0	Ideal-gas part of the non-dimensional Helmholtz free energy
α^r	Residual part of the non-dimensional Helmholtz free energy (real-fluid effects)
α^t	Total non-dimensional Helmholtz free energy, $\alpha^t = \alpha^0 + \alpha^r$
β	Thermal expansion coefficient $[K^{-1}]$
δ	Kronecker delta
ε	Turbulent kinetic energy dissipation rate $[m^2\ s^{-3}]$
γ	Ratio of specific heats, C_p/C_v
κ_T	Isothermal compressibility $[Pa^{-1}]$
λ	Thermal conductivity $[W\ m^{-1}\ K^{-1}]$
μ	Dynamic viscosity $[Pa\ s]$
ρ	Density $[kg\ m^{-3}]$
θ	Runge-Kutta weighting coefficients
ϕ	Generic nondimensional thermodynamic property
τ_{ij}	Viscous stress tensor component in direction i acting on the face normal to direction j $[Pa]$

$\mathscr{F}$	Equation of state function
$\mathscr{R}(p_0)$	Residual function for mass conservation $[kg]$
$\mathscr{R}'(p_0)$	Derivative of residual function with respect to p_0 $[kg\ Pa^{-1}]$
Ω	Computational domain $[m^3]$
Φ	Right-hand side of momentum transport equation $[m\ s^{-2}]$
Ψ	Right-hand side of energy equation $[J\ kg^{-1}\ s^{-1}]$

Abbreviations

CaNS	Canonical Navier-Stokes
DHC	Differential Heated Cavity
DNS	Direct Numerical Simulation
EoS	Equation of State
FFT	Fast Fourier Transform
IG	Ideal Gas
LES	Large Eddy Simulation
R.E.	Richardson Extrapolation
RANS	Reynolds-Averaged Navier–Stokes
sCO_2	Supercitical carbon dioxide
WENO	Weighted Essentially Non-Oscillatory

Chapter 1

Introduction

Over the past century, the global energy landscape has undergone several transformations driven by the need to reduce greenhouse gas emissions, increase energy efficiency, and transition to more sustainable technologies. In this context, optimizing energy conversion systems has become a key challenge in scientific research and industrial development. One of the most promising approaches in this field is the use of supercritical fluids, which enable compact, high efficiency heat transfer and power generation systems.

Thermal systems rely on mechanisms of energy exchange to convert heat into work or exchange heat between components. Convective transport in closed-loop systems has received growing attention due to its relevance in applications such as supercritical Rankine cycles, refrigeration systems, and next-generation nuclear reactors (Moran et al. (2010) [1]). Figure 1.1 illustrates the working principle of a typical Rankine cycle, highlighting the heat input, turbine work extraction, and heat rejection via condensation, all occuring in a closed loop system.

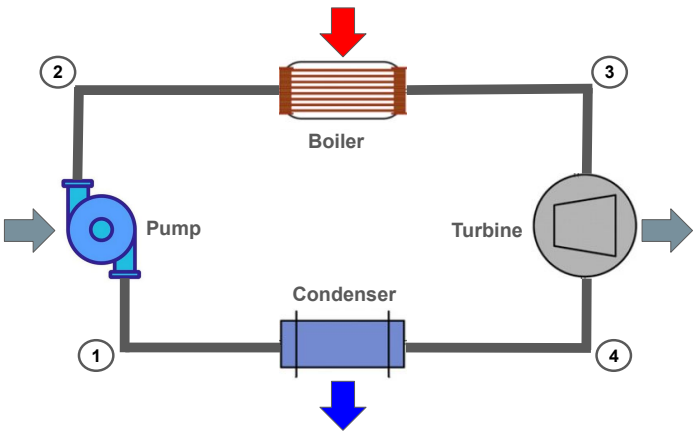

Figure 1.1: Schematic of a Rankine cycle. The red arrow denotes heat input to the boiler, the blue arrow denotes heat rejection at the condenser, and the gray arrows indicate work input to the pump and output from the turbine.

To gain deeper insight into the thermodynamic behavior of working fluids, Figures 1.2 and 1.3, adapted from Marzouk (2024) [2], illustrate the temperature–entropy diagrams for subcritical and supercritical Rankine cycles, respectively.

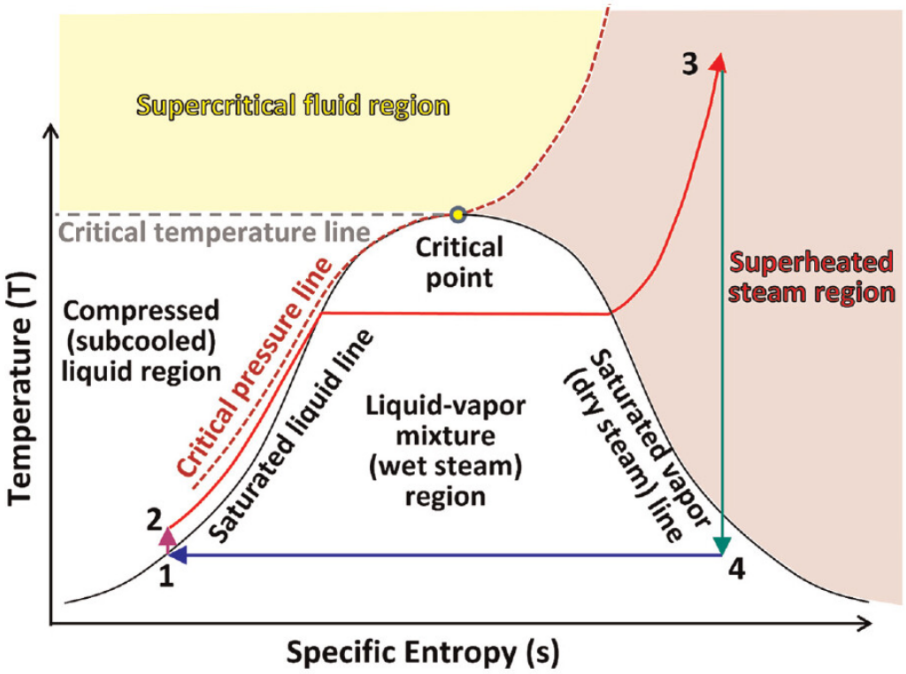

Figure 1.2: T–s diagram of a typical subcritical Rankine cycle. The cycle crosses the vapor–liquid saturation dome, involving phase change. Adapted from Marzouk (2024).

In the subcritical Rankine cycle, as represented in Figure 1.2, the working fluid undergoes a phase change as it crosses the vapor–liquid saturation dome. Heat is added at constant pressure, first leading to vaporization and then further heating in the vapor phase. This is followed by expansion through a turbine, heat rejection in a condenser, and compression in a pump to close the loop. This cycle relies on latent heat exchange and is constrained by isothermal heat addition, which can limit the maximum amount of work the system can produce or, in other terms, exergy.

In contrast, the supercritical Rankine cycle, as shown in Figure 1.3, operates above the saturated liquid line and reaches the supercritical regime, where the fluid no longer exhibits distinct liquid and vapor phases. As a result, the working fluid follows a continuous thermodynamic path with no phase change, and heat is transferred over a range of temperatures. This enables better thermal integration with external heat sources, and improves exergy recovery. The absence of phase change also simplifies the design of the heat exchanger and contributes to the compactness of the system and its operational flexibility.

Given these characteristics, supercritical cycles present a promising alternative to traditional subcritical systems. Their ability to accommodate gradual heat addition allows for more effective

use of low-grade or variable-temperature heat sources. Moreover, they offer higher thermal efficiencies, particularly when real-fluid effects are properly modeled and accounted for in the system design. Among potential working fluids, supercritical carbon dioxide (sCO_2) stands out due to its low critical temperature and pressure, environmental safety (non-toxic, non-flammable), and suitability for compact systems.

However, operating near the critical and critical regions introduces significant complexity in modeling and simulation. Although no phase change occurs, steep gradients in density, specific heat, viscosity, and other properties still exist and require accurate thermophysical models to capture local flow behavior and thermal performance. Advanced numerical methods and real-fluid equations of state are therefore essential to ensure reliable predictions and guide the design of efficient supercritical systems.

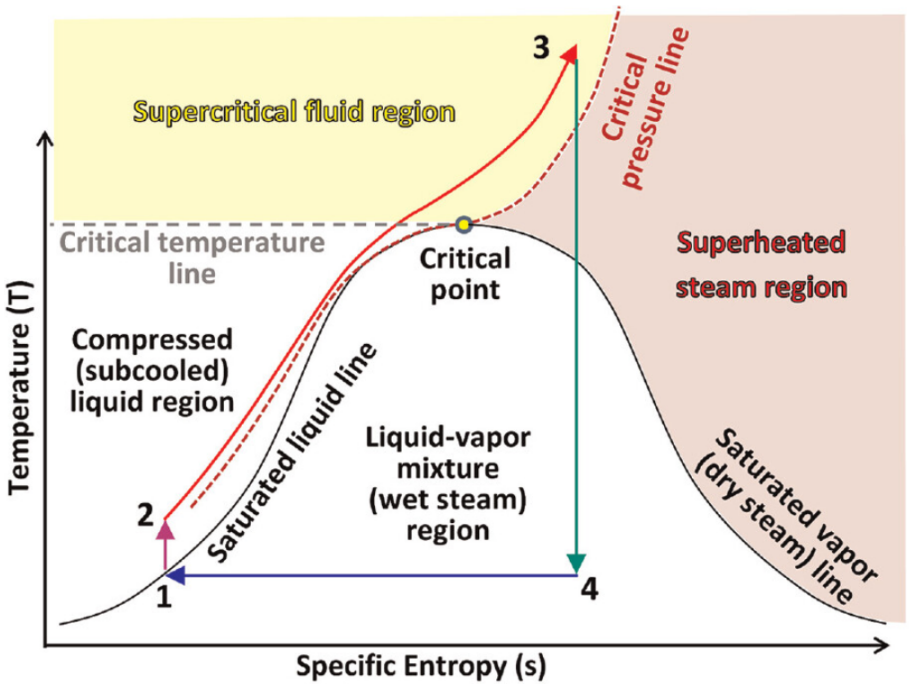

Figure 1.3: T–s diagram of a supercritical Rankine cycle. The working fluid avoids phase change by operating above the critical point. Adapted from Marzouk (2024).

The present work aims to advance the numerical modeling of real-fluid heat transfer and flow in closed systems by developing a solver capable of simulating these processes across a range of operating conditions and for different fluids, without phase change. Particular emphasis is placed on accurately capturing thermodynamic and transport property variations near the supercritical region, using governing equations formulated under the low Mach number approximation, which is appropriate for this class of flows.

This thesis is organized into eight chapters. Chapter 2 provides a review of the relevant literature, identifies the current research gap, and outlines the objective of this work. Chapter 3 introduces the reformulates governing equations and the adopted thermodynamic formulation. Chapter 4 describes the numerical implementation of the solver. Chapter 5 presents the validation of the numerical algorithm against reference cases. Chapter 6 details the setup of the numerical simulations performed, and Chapter 7 discusses the main results and the physical insights obtained. Finally, Chapter 8 summarizes the conclusions and proposes directions for future research.

Chapter 2

Literature Review

The low Mach number approximation has been used to simulate fluid flows in varied thermodynamic regimes, providing a computationally efficient alternative to fully compressible formulations of the Navier-Stokes equations by filtering out acoustic phenomena while retaining key thermodynamic couplings. As reported in existing research, this approach has been extensively applied to open systems involving real fluids, particularly in the supercritical regime, where sharp property gradients emerge near the critical point. In parallel, studies on closed systems have focused mainly on ideal gas, taking advantage of the simplifications offered by constant or moderately changing properties. However, the application of low Mach number models to closed systems involving real fluids remains limited. This represents a gap in the literature, as such configurations are relevant in numerous engineering and scientific contexts where property variations and confinement effects play a dominant role.

Supercritical fluids arise when a substance is subjected to temperatures and pressures above its critical point – a regime in which the distinction between liquid and gas phases vanishes. In this region, thermodynamic properties such as density, compressibility, and specific heat exhibit highly non-linear behavior, with abrupt variations in response to small changes in temperature or pressure. These steep gradients significantly influence flow dynamics, turbulence structures, and heat transfer mechanisms, making it essential to account for real-fluid effects in any physically consistent simulation. As shown in Figure 2.1, both the density and the speed of sound vary sharply near the critical point, highlighting the inadequacy of ideal gas assumptions under such conditions. Capturing these effects is very important for accurate modeling, particularly in systems operating near the critical point.

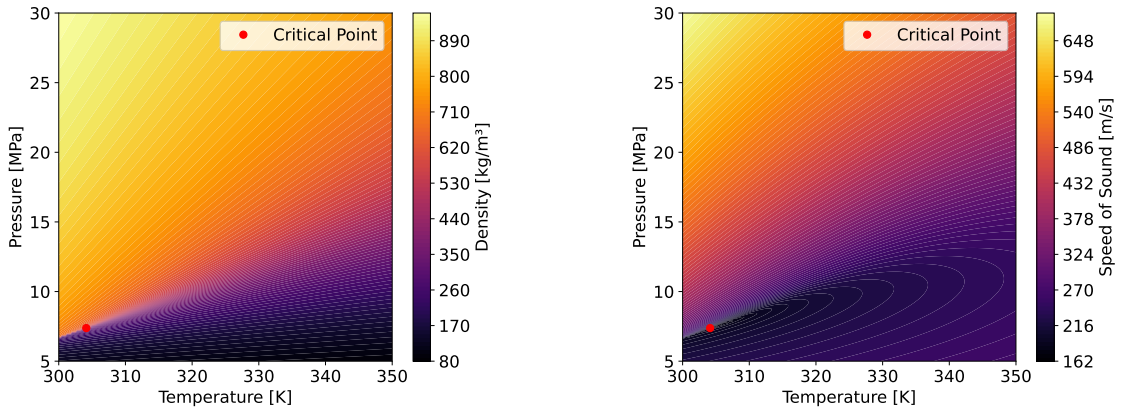

Density Speed of Sound

Figure 2.1: Thermodynamic property variation of sCO_2 near the critical point obtained using the CoolProp library.

Several key studies have shaped the understanding of heat transfer to supercritical fluids. One of the first reviews was by Petukhov (1968) [3], who highlighted discrepancies between experimental results and the correlations for skin friction and the Nusselt number available in cases with strong variations in thermophysical properties. On the same occasion, Hall et al. (1967) [4] reviewed empirical correlations for supercritical water and emphasized the need to account for property gradients and buoyancy effects.

2.1 Experimental studies

Experimental studies in the following decades, notably by Yamagata et al. (1972) [5] and Ackerman (1970) [6], investigated upward flows of heated supercritical water under imposed wall heat fluxes. Their findings showed that both heat transfer enhancement and deterioration occur in the vicinity of the pseudo-critical temperature – the temperature at which the heat capacity at constant pressure reaches its maximum for a given supercritical pressure. This region is strongly influenced by the applied heat flux and flow direction. These experiments revealed that the heat transfer coefficient typically reaches a local peak when the bulk temperature is near the pseudo-critical point, although this peak diminishes as the heat flux increases. The observed behaviors were attributed to buoyancy effects and thermal acceleration.

Subsequent experimental work by Kurganov and Kaptilnyi (1993) [7] expanded this understanding by examining turbulent sCO_2 flows in vertically heated tubes under mixed convection conditions. Their results highlighted that buoyancy-induced flow structure rearrangement plays a significant role in modulating heat transfer behavior, particularly in upward flows. A notable deterioration in heat transfer was observed when the wall temperature peak developed near the inlet, which was attributed to the suppression of turbulence generation in the fluid layer adjacent to the

wall. The study also quantified velocity profiles, shear stresses, eddy diffusivities, and turbulent Prandtl numbers, revealing discrepancies between experimental observations and conventional turbulence models.

Later, Pioro and Duffey (2005) [8] conducted a review of the literature, analyzing over 450 publications related to heat transfer in supercritical water flowing through different types of channels. Their survey showed that most experimental work focused on vertical and horizontal circular tubes, while studies involving annuli or bundle configurations were scarce. They identified three main heat transfer regimes under supercritical pressure conditions: (1) a standard regime, (2) a degraded regime with reduced heat transfer coefficients and elevated wall temperatures, and (3) an enhanced regime where heat transfer is intensified. A consistent increase in the heat transfer coefficient was observed near the critical and pseudo-critical temperatures. They also noted that deterioration is more likely to occur at high heat input and low mass flow, though this effect can be mitigated by increasing turbulence, for example, through the use of obstacles or enhancement techniques. Despite the extensive review, they pointed out the need for further research in more complex geometries to support the development of accurate design methodologies.

More recently, experiments by Xiong et al. (2012) [9] at the Nuclear Power Institute of China explored flow instability in supercritical water within parallel heated channels. By progressively increasing the heat flux, they identified stability boundaries and observed that higher inlet temperatures or total mass fluxes delay the onset of instability.

Additionally, a latest study by Li et al. (2023) [10] focused on the natural circulation heat transfer of sCO_2 in a closed loop. Their experiments identified two distinct heat transfer regimes: normal heat transfer and heat transfer deterioration. These regimes were shown to be strongly influenced by the variation of the thermophysical properties. They developed a new deterioration criterion based on a dimensionless parameter and found that the existing correlations of heat transfer from forced convection for sCO_2 are not directly applicable to natural circulation. They have also proposed a new correlation that significantly improves prediction accuracy.

2.2 Numerical studies

2.2.1 Pioneering computational approaches

On the computational side, early studies relied on Reynolds-averaged Navier-Stokes equations (RANS) models. Koshizuka et al. (1995) [11], using a k $-\varepsilon$ turbulence model, compared their results with experimental data from Yamagata et al. (1972) [5] and observed qualitative agreement, although the model failed to capture heat transfer deterioration. Further attempts to model supercritical heat transfer using RANS were made by Laurien (2010) [12], who focused on the development of wall functions and turbulence model parameters based on an analytical description of the near-wall turbulent and conductive sublayers under heat transfer deterioration conditions.

The study emphasized the need to account for local variations in the Prandtl number and enthalpy gradients, as well as buoyancy effects, in order to improve the accuracy of RANS predictions in deteriorated regimes. Several studies, including those by Wen & Gu (2010) [13], Kim et al. (2008) [14], and Jiang et al. (2006) [15], applied various turbulence models to simulate sCO_2 flow in different regimes. While these models qualitatively captured the trends of buoyancy-induced heat transfer deterioration, they tended to overpredict wall temperatures and failed to resolve finer details of the heat transfer behavior.

Despite some qualitative agreement, conventional turbulence models still show notable discrepancies in the predictions of wall temperature and heat transfer, revealing their limitations and the need for improved numerical approaches.

With advancements in computational power, DNS and large-eddy simulations (LES) have become instrumental in exploring these phenomena in greater detail. In their pioneering DNS study, Bae et al. (2005) [16] studied the convective heat transfer of sCO_2 in a vertical heated pipe by solving the fully compressible Navier–Stokes equations. Their work highlighted the strong influence of buoyancy effects, especially when the pseudo-critical temperature zone lies between the wall and the pipe centerline, a condition that triggers significant thermophysical property gradients. The results confirmed that buoyancy plays a key role in heat transfer behavior near the pseudo-critical temperature, supporting mechanisms of deterioration and recovery that are also relevant in horizontal channel flows.

2.2.2 Fundamentals of low Mach simulations

Despite the accuracy of the fully compressible formulation of the Navier-Stokes equations, it can be computationally expensive and inefficient, particularly for low-speed flows where acoustic effects are not dominant. In such regimes, a low Mach number approximation offers a more efficient alternative by filtering out sound waves while preserving key thermodynamic and hydrodynamic couplings.

The relevance of such approximations is conceptually supported by the hypothesis proposed by Morkovin (1962) [17], which states that in turbulent flows with low to moderate Mach numbers (up to Mach 5), the structure of turbulence remains essentially similar to that of incompressible flows, provided that mean property variations are properly accounted for. This idea, further supported by the numerical evidence of Coleman et al. (1995) [18], helps justify the use of incompressible-like turbulence models and simplified formulations in a wide range of compressible flows.

However, the formal derivation of low Mach number equations – commonly used in supercritical or thermally-driven flows – relies on a distinct asymptotic approach. A pivotal contribution in this context is the work of Majda and Sethian (1985) [19], who derived the governing equations for zero-Mach-number combustion. Their formulation serves as the theoretical basis for many

modern low Mach number solvers, enabling efficient simulation of thermally-driven phenomena without resolving acoustic waves.

As will be discussed later, the low Mach number approximation allows the total pressure to be decomposed as $p = p_0 + p_1$, where p_0 is the thermodynamic pressure, invariant in space, and p_1 is the hydrodynamic pressure that locally adjusts to enforce momentum conservation. In the most general formulation, we can write $p_0 = \mathrm{f}(t)$, $p_1 = \mathrm{f}(\mathbf{x},t)$ and $p_0 \gg p_1$.

2.2.3 Open-system configuration for real fluid effects: constant thermodynamic pressure assumption

Several DNS studies have used this low Mach number framework to explore heat transfer and turbulence in supercritical fluids. For example, turbulent jet flows of supercritical fluids have been the focus of several DNS studies, including those by Battista et al. (2014) [20], Creta et al. (2016) [21], Lapenna and Creta (2017) [22], and Lapenna et al. (2018) [23]. These studies also rely on the low Mach number approximation and assume temporally invariant thermodynamic pressure, justified by the open nature of the jet flow configuration, where boundary conditions enforce a fixed pressure level.

Similarly, Wang et al. (2023) [24] extended this approach to turbulent supercritical channel flows using a low Mach number solver under the assumption of an open system, thus considering a constant thermodynamic pressure over time. Other recent DNS efforts in open systems follow a similar strategy, focusing on capturing complex turbulence-thermodynamic interactions while avoiding the additional complexity of dynamically evolving pressure fields. However, this assumption limits the direct applicability of their findings to closed systems, where thermodynamic pressure should evolve over time to ensure mass and energy conservation.

2.2.4 Closed-system configuration for real fluid effects

In contrast, efforts to simulate closed supercritical systems using DNS are more limited. Peeters (2016) [25] employed a low Mach number solver to investigate the turbulent flow of sCO_2 in a vertically oriented, periodic annular domain with simultaneously heated and cooled walls. By considering the system as isolated – without net flux of mass or heat through the domain boundaries – they justified the use of a temporally invariant thermodynamic pressure ($dp_0/dt = 0$). This assumption is supported by integral energy balance arguments: under fully developed conditions, the net heat flux and enthalpy transport across the control volume vanish, leading to a steady thermodynamic state. The configuration enabled a focused analysis of how thermophysical property gradients and buoyancy-induced density stratification affect turbulence. In particular, turbulence was strongly attenuated near the heated inner wall, as indicated by a marked decrease in turbulent

shear stress. This suppression was attributed to stabilizing density stratification, which dampens turbulence generation and mixing.

Nemati (2016) [26] also used the low Mach number approximation for DNS of heated pipe flows with supercritical carbon dioxide, but instead of assuming constant thermodynamic pressure, they accounted for its time evolution. This was achieved by artificially adjusting the total mass in the system at each time step to maintain consistency with the governing equations and to close the problem in a thermodynamically consistent way. Their formulation computes the thermodynamic pressure dynamically based on global mass and energy conservation, enabling modeling of the system's temporal evolution. However, the total mass, which should ideally remain constant, fluctuates slightly over time, making this approach potentially unreliable for more complex systems. To capture real-fluid effects, they tested different equations of state (EoS) in their implementation, including cubic EoS such as Soave–Redlich–Kwong and Peng–Robinson, as well as multi-parameter EoS based on the Helmholtz free energy. These more advanced EoS, particularly the Helmholtz-based formulation by Span and Wagner (2003) [27], provided better agreement with reference databases near the critical region. The study highlighted that the choice of EoS significantly affects the prediction of thermodynamic and transport properties, and consequently, the overall fidelity of DNS simulations in supercritical regimes.

The choice of the EoS plays a critical role in the DNS of supercritical flows, as it governs how thermodynamic properties respond to pressure and temperature variations. Although early studies often employed cubic models like Peng–Robinson or Soave–Redlich–Kwong, more recent work has shifted toward Helmholtz-based multi-parameter EoS, such as the Span and Wagner (2003) [28] formulation, due to their improved accuracy near the critical point. Unlike cubic EoS, Helmholtz-based models can accurately capture complex phenomena such as sharp variations in density, specific heat, and other thermodynamic properties, which are critical for modeling flows in the near-critical regime. These models are typically implemented using libraries such as CoolProp [29] or REFPROP [30] and have been successfully integrated into DNS solvers, as shown by Nemati (2016) [26], to capture real-fluid effects with high fidelity.

While previous DNS studies have advanced our understanding of supercritical turbulent flows, a significant gap remains in the modeling of closed systems with real fluid effects, particularly with respect to the time evolution of the thermodynamic pressure. Most existing approaches either assume constant thermodynamic pressure or adopt ideal gas simplifications, which are inadequate for accurately capturing the coupled mass, momentum, and energy transport equations in fully enclosed, thermodynamically consistent configurations. This raises the central research question of the present work:

How can the low Mach number formulation be extended to enable direct numerical simulation of closed systems while rigorously accounting for real-fluid behavior?

To address this question, the objective of this study is to develop and implement a general low Mach number solver that analytically imposes global conservation laws to compute the time-dependent thermodynamic pressure, while incorporating real-fluid effects through high-fidelity Helmholtz-based equations of state. This enables a physically consistent DNS of closed domains operating in supercritical regimes, offering a more robust and accurate framework than previous approximations.

Chapter 3

Mathematical Formulation

The fully compressible Navier-Stokes equations coupled with an EoS provide a complete mathematical framework for describing fluid motion in any regime. However, solving them can be computationally expensive and time-consuming. This is mainly due to the strict time-step constraints imposed by the high value of the speed of sound, since pressure waves are responsible for transmitting information throughout the domain. When the characteristic velocity of the fluid is much lower than the speed of sound in the medium, it becomes possible to simplify the equations by neglecting certain physical phenomena that are not relevant to the dynamics of interest. The low Mach number approximation is one such simplification used in this work. In this formulation, the density changes resulting from pressure disturbances related to compressibility are not considered. However, density variations arising from thermal effects, such as temperature gradients, are still captured.

This chapter begins with an overview of the low Mach number approximation. The fundamental governing equations are then presented, along with the reference scales adopted for nondimensionalization and the dimensionless numbers that emerge naturally from this process. The low Mach number assumption is incorporated directly into the equations to simplify the system by filtering out acoustic effects. After this, the equations are redimensionalized to restore a clearer physical interpretation. It is important to note that although the equations are presented in dimensional form for clarity, the numerical implementation was developed entirely using nondimensional variables. The chapter concludes with a detailed discussion of two important constraints of the system and the methodology used to evaluate the thermodynamic properties.

3.1 Low Mach number approximation

The low Mach number approximation seeks to suppress acoustic wave propagation while preserving the key thermodynamic and transport phenomena of the flow. By filtering out sound

waves, this method effectively decouples thermodynamics from hydrodynamic pressure, removing acoustic effects from the simulation and allowing density and other thermophysical properties to be treated as functions of temperature and thermodynamic pressure alone.

The method is based on expanding all dependent variables in a power series of M^2 and then reducing the governing equations to their leading-order terms in M^2. For example, pressure is written as $p = p_0 + (M^2)p_1 + (M^2)^2 p_2 + ...$, and similar expansions are applied to other variables such as density, velocity, and temperature. The reason behind this approach, derived in more detail in Appendix A, is to express the pressure as the sum of a thermodynamic component p_0 and a hydrodynamic component p_1. This separation ensures that the thermodynamic pressure does not affect momentum transport while the hydrodynamic pressure does not influence the thermodynamic properties. During the derivation of the low Mach number equations, it naturally follows that the thermodynamic pressure does not vary in space,

$$\frac{\partial p_0}{\partial x_j} = 0 \quad \Longrightarrow \quad \frac{\partial p_0}{\partial t} = \frac{dp_0}{dt}. \tag{3.1}$$

It is important to note that the thermodynamic pressure, p_0, may still vary over time, as we are considering a closed system. In contrast, for an open system, this pressure remains constant both in space and time, being equal to the ambient (e.g., atmospheric) pressure.

3.2 Governing equations

The general formulation of the fully compressible Navier-Stokes equations, capturing the conservation of mass, momentum, and energy, as well as the equation of state for real fluids in dimensional form reads (Poinsot and Veynante (2005) [31]):

$$\frac{\partial \rho}{\partial t} + \frac{\partial}{\partial x_i}(\rho u_i) = 0, \tag{3.2}$$

$$\frac{\partial}{\partial t}(\rho u_j) + \frac{\partial}{\partial x_i}(\rho u_i u_j) = -\frac{\partial p}{\partial x_j} + \frac{\partial \tau_{ij}}{\partial x_i} + \rho f_j, \tag{3.3}$$

$$\frac{\partial \rho h_t}{\partial t} + \frac{\partial}{\partial x_i}(\rho u_i h_t) = \frac{\partial p}{\partial t} - \frac{\partial q_i}{\partial x_i} + \frac{\partial}{\partial x_j}(\tau_{ij} u_i) + \dot{Q}, \tag{3.4}$$

$$\mathscr{F}(T,\ p,\ \rho) = 0. \tag{3.5}$$

Here, ρ denotes the fluid density, u_i the velocity components, p the total pressure, τ_{ij} the viscous stress tensor (momentum diffusion due to velocity gradients), f_j an external force per unit mass, $\dot{Q}$ the volumetric heat source and T the temperature. The total enthalpy h_t is defined as $h_t = e_t + p/\rho$, where the total energy per unit mass e_t includes both the sensible internal energy e

and the kinetic energy term $(u_i u_i)/2$. The heat flux vector q_i accounts for thermal conduction and is defined by Fourier's law as $q_i = -\lambda \partial T/\partial x_i$, where λ is the thermal conductivity.

To apply the low Mach number approximation, the following nondimensional variables are introduced:

$$\begin{aligned} \tilde{x} &= \frac{x}{L}, \quad \tilde{t} = \frac{t u_0}{L}, \quad \tilde{u_i} = \frac{u_i}{u_0}, \quad \tilde{\rho} = \frac{\rho}{\rho_0}, \quad \tilde{T} = \frac{T}{T_0}, \\ \tilde{p} &= \frac{p}{\rho_0 a_0^2}, \quad \tilde{\mu} = \frac{\mu}{\mu_0}, \quad \tilde{\lambda} = \frac{\lambda}{\lambda_0}, \quad \tilde{h}_t = \frac{h_t}{a_0^2}, \quad \tilde{f}_j = \frac{f_j L}{u_0^2}. \end{aligned} \tag{3.6}$$

where L is the reference length, u_0 is the reference velocity, ρ_0 is the reference density, T_0 is the reference temperature, a_0 is the reference speed of sound, μ_0 is the reference dynamic viscosity, and λ_0 is the reference thermal conductivity.

The fundamental idea behind this nondimensionalization is to choose the reference enthalpy as the square of the reference speed of sound. This approach is particularly well-suited for regimes where the speed of sound remains significantly higher than the characteristic flow velocity, ensuring the validity of the low Mach number approximation. However, the formulation becomes inappropriate near the critical point of a substance, where the speed of sound approaches zero and dynamic compressibility effects dominate. In such conditions, the underlying assumptions of this model break down, and a more complex multiphase framework would be required. Outside of this limitation, the method remains broadly applicable to a wide range of real-fluid scenarios, including both supercritical and other single-phase real-fluid conditions, as long as the speed of sound remains sufficiently large compared to the characteristic flow velocity of the system. In the same line of thought, the pressure is nondimensionalized by $\rho_0 a_0^2$, which represents the characteristic dynamic pressure scale in compressible flows. With this choice, both pressure, kinetic-energy, and enthalpy terms appear at the same order of magnitude in the nondimensional equations, avoiding the introduction of large stiff factors.

The nondimensional numbers that arise from this scaling are defined as:

$$Re_0 = \frac{\rho_0 u_0 L}{\mu_0}, \quad Pe_0 = \frac{\rho_0 u_0 L}{\lambda_0 T_0}, \quad M_0 = \frac{u_0}{a_0}, \quad Ra_0 = \frac{\Delta\rho L^3 g}{\mu \alpha}, \tag{3.7}$$

where Re_0 is the reference Reynolds number, Pe_0 is the reference Péclet number, M_0 is the reference Mach number, Ra_0 is the reference Rayleigh number based on the reference conditions, g is the magnitude of the gravitational acceleration vector, and α represents the thermal diffusivity, defined as $\lambda/(\rho\, C_p)$.

To derive the low Mach number formulation, the governing equations are first nondimensionalized using the mentioned reference scales. Since the Mach number is much smaller than

unity ($M \ll 1$), the kinetic energy contribution in the total enthalpy becomes negligible compared to the sensible enthalpy. Thus, the dimensionless total enthalpy can be approximated by the sensible enthalpy alone. Subsequently, the enthalpy transport equation is rewritten in terms of temperature T, by expressing the sensible enthalpy as a function of temperature and pressure, $h_t = h_t(T, p)$ (this step plays an important contribution of this work as will be further discussed). Finally, the dependent variables are expanded in a power series of the Mach number squared, M^2, and only the leading-order terms are retained. For example, pressure is written as $p = p_0 + (M^2)p_1 + (M^2)^2 p_2 + ...$, and similar expansions are applied to other variables such as density, velocity, and temperature. This yields the nondimensional governing equations under the low Mach number approximation. In this framework, the thermodynamic properties such as the specific heat at constant pressure, isothermal compressibility, and the thermal expansion coefficient, respectively,

$$C_p = \left(\frac{\partial h}{\partial T}\right)_p, \quad \kappa_T = \frac{1}{\rho}\left(\frac{\partial \rho}{\partial p}\right)_T, \quad \beta = -\frac{1}{\rho}\left(\frac{\partial \rho}{\partial T}\right)_p,$$

emerge naturally from the equations to model the behavior of the real fluid. After applying the nondimensionalization process to the equations, they read as follows,

$$\frac{\partial \tilde{\rho}}{\partial \tilde{t}} + \frac{\partial}{\partial \tilde{x}_i}(\tilde{\rho}\tilde{u}_i) = 0, \tag{3.8}$$

$$\frac{\partial}{\partial \tilde{t}}(\tilde{\rho}\tilde{u}_j) + \frac{\partial}{\partial \tilde{x}_i}(\tilde{\rho}\tilde{u}_i\tilde{u}_j) = -\frac{\partial \tilde{p}_1}{\partial \tilde{x}_j} + \frac{1}{Re}\frac{\partial \tilde{\tau}_{ij}}{\partial \tilde{x}_i} + Ra\,\frac{\mu\alpha}{L^3 U_0^2}\,\frac{\rho_0}{\Delta\rho}\,\tilde{\rho}\,\delta_{j,3}, \tag{3.9}$$

$$\tilde{\rho}\tilde{C}_p\left[\frac{\partial \tilde{T}}{\partial \tilde{t}} + \tilde{u}_i\frac{\partial \tilde{T}}{\partial \tilde{x}_i}\right] = \tilde{\beta}\;\tilde{T}\;\frac{d\tilde{p}_0}{d\tilde{t}} + \frac{1}{Pe}\frac{\partial}{\partial \tilde{x}_i}\left(\tilde{\lambda}\;\frac{\partial \tilde{T}}{\partial \tilde{x}_i}\right), \tag{3.10}$$

$$\tilde{\mathscr{F}}(\tilde{p},\;\tilde{p}_0,\;\tilde{\rho}) = 0. \tag{3.11}$$

Note that δ is the Kronecker delta. These equations form the basis for the low Mach number formulation adopted in this work, where acoustic effects are filtered out and the thermodynamic pressure $p_0(t)$ is only time dependent. The appearance of the factor $\tilde{\beta}\;\tilde{T}$ before the $d\tilde{p}_0/d\tilde{t}$ term results directly from treating the enthalpy as a function of both temperature and pressure, $h_t = h_t(T, p)$, as it is appropriate for a real fluid. A common simplification in the literature for the general low Mach formulation is to assume $h = C_p T$, thereby neglecting the pressure dependence and considering enthalpy as a function of temperature only (in which case the factor $\tilde{\beta}\;\tilde{T}$ vanishes from the equations). Appendix A describes the entire process of the derivation of the dimensional low Mach approximation, including the formulation of the enthalpy treatment adopted in this work for real fluids.

It should be noted that all variables, except pressure, correspond to leading order (zero-th order) terms. In the present work, the flow development inside a differentially heated cavity will be considered, where the left and right vertical walls are held at constant but different temperatures, while the top and bottom boundaries are thermally insulated. Since no internal heat generation is present, the volumetric source term is omitted from the governing equations.

As previously mentioned, in order to better interpret the physics behind the equations, the system is re-dimensionalized:

$$\frac{\partial \rho}{\partial t} + \frac{\partial}{\partial x_i}(\rho\, u_i) = 0, \tag{3.12}$$

$$\frac{\partial}{\partial t}(\rho\, u_j) + \frac{\partial}{\partial x_i}(\rho\, u_i\, u_j) = -\frac{\partial p_1}{\partial x_i} + \frac{\partial \tau_{ij}}{\partial x_j} + \rho\; g_j, \tag{3.13}$$

$$\rho\, C_p \left[\frac{\partial T}{\partial t} + u_i \frac{\partial T}{\partial x_i}\right] = \beta\, T\, \frac{dp_0}{dt} + \frac{\partial}{\partial x_i}\left(\lambda\; \frac{\partial T}{\partial x_i}\right), \tag{3.14}$$

$$\mathscr{F}(T,\; p_0,\; \rho) = 0. \tag{3.15}$$

At this stage, the system contains seven unknowns: the three components of velocity (u, v, w), temperature T, thermodynamic pressure p_0, hydrodynamic pressure p_1, and density ρ. These are governed by six equations: the three momentum transport equations (one for each spatial direction), Eq. (3.13), the temperature transport equation, Eq. (3.14), the continuity equation, Eq. (3.12) and the equation of state, Eq. (3.15). To fully close the system, an additional relation is required. In the context of closed domains, this missing constraint is naturally provided by the global conservation of mass: the total mass enclosed within the system must remain invariant in time. This constraint is mathematically expressed by the following integral condition:

$$m_0 = \int_V \rho(p_0, T)\, dV = \text{Const.} \tag{3.16}$$

Although conceptually straightforward, this condition plays a key role in allowing the simulation of closed configurations involving real fluids. In these cases, the density ρ is a nonlinear function of both pressure and temperature. As such, ensuring that Eq. (3.16) is satisfied at each time step requires a consistent and accurate numerical update of the thermodynamic pressure p_0. The implementation of this constraint, therefore, is not merely auxiliary - it is one of the central mechanisms that allows the system to remain physically closed while accommodating strong thermodynamic variations.

In contrast, open systems are typically modeled by prescribing p_0 directly, treating it as a known and constant quantity. This approach removes the need to enforce mass conservation explicitly and is often sufficient when the flow interacts with an ambient environment.

3.3 Constraints for velocity divergence and thermodynamic pressure evolution

Reformulating the governing equations to isolate how p_0 changes with time and the velocity divergence is essential for numerical implementation. As will be shown in Chapter 4, these reformulations lead directly to auxiliary equations that govern the evolution of pressure and ensure compatibility with mass conservation. The derivations of these expressions represent one of the key methodological contributions of this work. For clarity, the final forms of the constraints are first presented and discussed in the following two subsections, before their full derivation is provided in subsection 3.3.3.

3.3.1 Velocity divergence constraint

For a closed system, combining Eq. (3.12), Eq. (3.14), and Eq. (3.15) yields a constraint on the velocity divergence. The velocity field is enforced by hydrodynamic pressure, as will be clear in the next chapter. The divergence of the velocity field for a closed system is given by,

$$\frac{\partial u_i}{\partial x_i} = \frac{\beta}{\rho C_p}\frac{\partial}{\partial x_i}\left(\lambda \frac{\partial T}{\partial x_i}\right) - \frac{\kappa_T}{\gamma}\frac{dp_0}{dt}, \tag{3.17}$$

with $\kappa_T = (1/\rho)(\partial\rho/\partial p)_T$ being the isothermal compressibility, which quantifies the relative variation of the density with pressure at constant temperature, and γ defined as the ratio between the specific heat at constant pressure and the specific heat at constant volume, C_p/C_v.

This constraint ensures that the mass conservation is satisfied even though the pressure field is split into a thermodynamic and a hydrodynamic component. The term involving dp_0/dt accounts for the compressibility effects due to thermal expansion or contraction, while the first term reflects the influence of heat diffusion.

3.3.2 Time evolution of the thermodynamic pressure

To obtain an explicit expression for the time evolution of the thermodynamic pressure, Eq. (3.17) is integrated over the entire computational domain. Considering that, in our closed systems, no-penetration/periodic boundary conditions (what comes in needs to come out of the domain) are applied at the boundaries, the volume integral of the divergence of the velocity field vanishes due to the divergence theorem:

$$\int_\Omega \frac{\partial u_i}{\partial x_i} dV = \int_{\partial\Omega} u_i n_i dS = 0. \tag{3.18}$$

Applying this condition to Eq. (3.17), dp_0/dt can be isolated as:

$$\frac{dp_0}{dt} = \frac{\displaystyle\int_\Omega \frac{\beta}{\rho C_p} \frac{\partial}{\partial x_i}\left(\lambda \frac{\partial T}{\partial x_i}\right) dV}{\displaystyle\int_\Omega \frac{\kappa_T}{\gamma} dV}. \tag{3.19}$$

This relation shows how the thermodynamic pressure evolves in time in response to both thermal diffusion and transport of thermodynamic properties.

It is important to note that in the limit of vanishing thermal diffusivity the thermodynamic pressure remains constant and the velocity field is divergence-free. This corresponds to an incompressible-like behavior, where the thermodynamic pressure remains constant in time and the flow becomes divergence-free.

The present formulation is particularly relevant in the case of real fluids, where properties such as ρ, C_p, β, and κ_T may vary significantly with temperature and pressure. The accuracy of this approach relies on an adequate resolution of these property gradients and on a consistent numerical scheme for their spatial discretization, which are discussed in Chapter 4.

3.3.3 Detailed derivation of both constraints

First, the time and spatial derivatives of temperature are expressed in terms of density and pressure, the total derivative is used:

$$\frac{\partial T}{\partial t} = \left(\frac{\partial T}{\partial \rho}\right)_{p_0} \frac{\partial \rho}{\partial t} + \left(\frac{\partial T}{\partial p_0}\right)_{\rho} \frac{\partial p_0}{\partial t}, \tag{3.20}$$

$$\frac{\partial T}{\partial x_j} = \left(\frac{\partial T}{\partial \rho}\right)_{p_0} \frac{\partial \rho}{\partial x_j} + \left(\frac{\partial T}{\partial p_0}\right)_{\rho} \frac{\partial p_0}{\partial x_j}. \tag{3.21}$$

Substituting these two expressions into Eq. (3.14),

$$\rho c_p \left[\left(\frac{\partial T}{\partial \rho}\right)_{p_0} \left(\frac{\partial \rho}{\partial t} + u_j \frac{\partial \rho}{\partial x_j}\right) + \left(\frac{\partial T}{\partial p_0}\right)_{\rho} \left(\frac{\partial p_0}{\partial t} + u_j \frac{\partial p_0}{\partial x_j}\right)\right] = \beta T \frac{dp_0}{dt} + \frac{\partial}{\partial x_i}\left(\lambda \frac{\partial T}{\partial x_i}\right). \tag{3.22}$$

Since p_0 is uniform in space, this simplifies to:

$$\rho c_p \left[\left(\frac{\partial T}{\partial \rho} \right)_{p_0} \left(\frac{\partial \rho}{\partial t} + u_j \frac{\partial \rho}{\partial x_j} \right) + \left(\frac{\partial T}{\partial p_0} \right)_{\rho} \frac{dp_0}{dt} \right] = \beta T \frac{dp_0}{dt} + \frac{\partial}{\partial x_i} \left(\lambda \frac{\partial T}{\partial x_i} \right). \tag{3.23}$$

Introducing the continuity equation:

$$\frac{\partial \rho}{\partial t} + u_j \frac{\partial \rho}{\partial x_j} = -\rho \frac{\partial u_j}{\partial x_j}. \tag{3.24}$$

Substituting this into Eq. (3.23):

$$\rho c_p \left[-\left(\frac{\partial T}{\partial \rho} \right)_{p_0} \rho \frac{\partial u_j}{\partial x_j} + \left(\frac{\partial T}{\partial p_0} \right)_{\rho} \frac{dp_0}{dt} \right] = \beta T \frac{dp_0}{dt} + \frac{\partial}{\partial x_i} \left(\lambda \frac{\partial T}{\partial x_i} \right). \tag{3.25}$$

Isolating the divergence of velocity:

$$\frac{\partial u_j}{\partial x_j} = -\frac{1}{\rho \left(\frac{\partial T}{\partial \rho} \right)_{p_0}} \left[\frac{1}{\rho c_p} \left(\beta T \frac{dp_0}{dt} + \frac{\partial}{\partial x_i} \left(\lambda \frac{\partial T}{\partial x_i} \right) \right) - \left(\frac{\partial T}{\partial p_0} \right)_{\rho} \frac{dp_0}{dt} \right]. \tag{3.26}$$

Using the previously mentioned thermodynamic relations:

$$\left(\frac{\partial T}{\partial \rho} \right)_{p_0} = -\frac{1}{\rho \beta}, \qquad \left(\frac{\partial T}{\partial p_0} \right)_{\rho} = \frac{\kappa_T}{\beta}. \tag{3.27}$$

and substituting them in Eq. (3.26), the divergence becomes:

$$\frac{\partial u_j}{\partial x_j} = \beta \left[\frac{1}{\rho c_p} \left(\beta T \frac{dp_0}{dt} + \frac{\partial}{\partial x_i} \left(\lambda \frac{\partial T}{\partial x_i} \right) \right) - \frac{\kappa_T}{\beta} \frac{dp_0}{dt} \right]. \tag{3.28}$$

Multiplying both sides by ρc_p, yields:

$$\rho c_p \frac{\partial u_j}{\partial x_j} = \beta \frac{\partial}{\partial x_i} \left(\lambda \frac{\partial T}{\partial x_i} \right) + \left(\beta^2 T - \rho c_p \kappa_T \right) \frac{dp_0}{dt}. \tag{3.29}$$

Using the general thermodynamic relation $c_p - c_v = \frac{\beta^2 T}{\rho \kappa_T}$ (Gaskell (2008) [32]),

$$\frac{\beta^2 T}{\rho c_p} = \kappa_T \left(1 - \frac{c_v}{c_p} \right) = \kappa_T \left(1 - \frac{1}{\gamma} \right), \tag{3.30}$$

Substituting this relation into Eq. (3.29), the velocity divergence constraint can be written in its final form as:

$$\frac{\partial u_j}{\partial x_j} = \frac{\beta}{\rho c_p}\frac{\partial}{\partial x_i}\left(\lambda\frac{\partial T}{\partial x_i}\right) - \frac{\kappa_T}{\gamma}\frac{dp_0}{dt}, \tag{3.31}$$

By integrating the velocity divergence constraint over the entire computational domain, an expression for the time evolution of the thermodynamic pressure can be obtained. Assuming periodic boundary conditions at the boundaries where flow can cross, the volume integral of the velocity divergence vanishes due to the divergence theorem:

$$\int_\Omega \nabla\cdot\mathbf{u}\,dV = 0. \tag{3.32}$$

The final expression for the pressure time derivative reads:

$$\frac{dp_0}{dt} = \frac{\int_\Omega \frac{\beta}{\rho c_p}\nabla\cdot(\lambda\nabla T)\,dV}{\int_\Omega \frac{\kappa_T}{\gamma}\,dV}. \tag{3.33}$$

3.4 Equation of state

To accurately represent the thermophysical properties of the working fluid, an EoS beyond the ideal gas law is required. In this work, fluid properties are evaluated using CoolProp, an open source reference-quality thermophysical property library developed by Bell et al. (2014) [29].

The fundamental thermodynamic potential used in CoolProp is the nondimensional Helmholtz free energy α^t, which is decomposed into two components:

$$\alpha^t = \alpha^0 + \alpha^r, \tag{3.34}$$

where α^0 is the contribution of the ideal gas and α^r is the residual part that accounts for the effects of the real fluid. From this formulation, all other thermodynamic properties can be obtained through analytic derivatives of terms α^0 and α^r.

Chapter 4

Implementation

This chapter focuses on the computational aspects of implementing governing equations in the low Mach number limit, as discussed in the previous chapter. The starting point is the incompressible flow solver developed by Costa (2018) [33], known as CaNS, which solves the constant-coefficient Poisson equation for pressure using the Fast Fourier Transform (FFT). This framework was later extended by Kottursheltar (2023) [34] into a low Mach number solver capable of handling large density variations, under the assumption of an ideal gas, for the study of stably stratified turbulent channel flows. In the present work, the solver from Kottursheltar (2023) [34] is further modified to incorporate real-fluid effects. This involves the reformulation of the governing equations, the implementation of a Newton-Raphson procedure to compute the thermodynamic pressure in a thermodynamically consistent manner for a closed system, and the integration of the CoolProp library to calculate thermodynamic properties.

4.1 Discretization schemes

The spatial discretization is based on a second-order finite-volume method applied over a staggered Cartesian grid where the velocity components are defined at the cell faces, while scalar fields such as temperature and pressure reside at the cell centers. The diffusive terms of both the momentum and energy equations are discretized using second-order central differences. However, to improve stability and accuracy in regions with sharp thermal gradients, the advective terms in the energy equation are discretized using a third-order Weighted Essentially Non-Oscillatory (WENO) scheme (Jiang and Shu (1996) [35]). The key idea of the WENO method is to interpolate the temperature directly using a weighted combination of lower-order polynomials, with the weights favoring smooth stencils and avoiding oscillations near discontinuities. To compute the velocity field at the time level $n+1$, a three-stage Runge-Kutta method is employed. Within each Runge-Kutta substep k, the following quantities are sequentially updated: the temperature field, the time derivative of the thermodynamic pressure dp_0/dt, the thermodynamic pressure itself, the thermophysical properties, the hydrodynamic pressure, and finally the velocity field. This process is described in detail below.

To advance the simulation in time, Wray's low-storage third-order Runge-Kutta method is employed (Kennedy et al. (2000) [36]). At each Runge-Kutta stage $k+1$, the temperature field is updated through:

$$T^{k+1} = T^k + \Delta t\, \theta^k \Psi(T^k). \tag{4.1}$$

where θ^k are the Runge–Kutta coefficients and Ψ contains the convective and diffusive terms of the temperature transport equation for a real fluid,

$$\Psi(T) = -u_j^k \frac{\partial T^k}{\partial x_j} + \frac{1}{\rho^k C_p^k} \frac{\partial}{\partial x_i} \cdot (\lambda^k \frac{\partial T^k}{\partial x_i}) + \frac{\beta^k}{\rho^k C_p^k} T^k \left(\frac{dp_0}{dt} \right)^k. \tag{4.2}$$

In this formulation, different terms in the equations are integrated in time using distinct numerical approaches to balance stability and efficiency. The horizontal advection and diffusion terms are treated explicitly at each Runge-Kutta stage, while the vertical (wall-normal) diffusion term is handled implicitly using the Crank-Nicolson method. This mixed approach allows for larger time steps without compromising numerical stability, particularly in regions with refined mesh in the vertical direction.

The term dp_0/dt is calculated from the global mass conservation constraint in closed domains, as expressed in Eq. (3.19). This coupling ensures that the thermodynamic pressure evolves consistently with the imposed divergence constraint and the real-fluid equation of state.

To determine the thermodynamic pressure at the new time step, in a closed system with real fluid behavior, it is necessary to enforce global mass conservation as expressed in Eq. (3.16). This constraint is mathematically expressed as:

$$\mathscr{R} = 0, \quad \text{with} \quad \mathscr{R}(p_0) = m_0 - \int_V \rho(p_0, T)\, dV, \tag{4.3}$$

where m_0 is the total mass of the system, assumed constant over time. The function $\mathscr{R}(p_0)$ reflects the difference between the imposed total mass and the instantaneous mass computed from the equation of state, which depends both on pressure and temperature.

To find the root of $\mathscr{R}(p_0)$, the Newton–Raphson method is implemented, resulting in the iterative formula:

$$p_0^{n_{NR}} = p_0^{n_{NR}-1} - \frac{\mathscr{R}(p_0^{n_{NR}-1})}{\mathscr{R}'(p_0^{n_{NR}-1})}, \tag{4.4}$$

where n_{NR} is a Newton-Raphson iteration and the derivative $\mathscr{R}'(p_0)$ with respect to pressure is given by:

$$\mathscr{R}'(p_0) = \left(\frac{\partial \mathscr{R}}{\partial p_0}\right)_T = \frac{\partial}{\partial p_0}\left(\int_V \rho(p_0, T)\, dV\right)_T = \int_V \left(\frac{\partial \rho}{\partial p_0}\right)_T dV = \int_V \rho\, \kappa_T\, dV. \tag{4.5}$$

Substituting Eq. (4.3) and Eq. (4.5) into the Newton–Raphson expression yields the following formula to update the thermodynamic pressure:

$$p_0^{n_{NR}} = p_0^{n_{NR}-1} - \frac{m_0 - \int_V \rho(p_0^{n_{NR}-1}, T)\, dV}{\int_V \rho(p_0^{n_{NR}-1}, T)\, \kappa_T(p_0^{n_{NR}-1}, T)\, dV}. \tag{4.6}$$

This iterative procedure ensures that the thermodynamic pressure is consistent with mass conservation at each time step while accounting for the effects of the real fluid through the equation of state.

Once the temperature and the thermodynamic pressure are determined, all remaining thermodynamic properties can be updated using the CoolProp library, which was integrated into the Fortran code using the `ISO_C_BINDING` interface (Bell et al. (2014) [29]).

In order to reduce the computational cost associated with repeated calls to the CoolProp library during the simulation, thermodynamic properties such as ρ, C_p, μ, λ, β and κ_T were precomputed over a uniform two-dimensional grid of temperature and pressure values and stored in a look-up table. During the simulation, the required property values at each temperature and pressure points were obtained through interpolation across these precomputed tables.

Rinaldi (2015) [37] compared the performance of three interpolation methods - including bilinear interpolation, least-squares gradient interpolation, and third-order polynomial Lagrange interpolation - for sCO_2 flows. His results showed that third-order polynomial Lagrange interpolation offers superior accuracy, particularly in regions with steep property gradients. On the basis of these findings, a third-order polynomial Lagrange interpolation scheme was adopted in the present work for the evaluation of thermodynamic properties.

The interpolation for a generic nondimensional property ϕ at a given point (T, p) is performed as:

$$\phi(T, p) = \sum_{i=1}^{4}\sum_{j=1}^{4}\left(\prod_{\substack{m=1\\m\neq i}}^{4}\frac{T - T_m}{T_i - T_m}\right)\left(\prod_{\substack{n=1\\n\neq j}}^{4}\frac{p - p_n}{p_j - p_n}\right)\phi(T_i, p_j), \tag{4.7}$$

where T_i and p_j represent the coordinates of the four neighboring temperature and pressure nodes, respectively, and $\phi(T_i, p_j)$ is the stored property value at each node.

To compute the velocity field at each time step, a pressure projection method is used. In the first stage, an intermediate velocity field u_i^* is obtained by explicitly integrating the momentum equation without the contribution of the pressure gradient. This is expressed as:

$$u_i^* = \frac{\rho^k}{\rho^{k+1}} u_i^k + \frac{\Delta t}{\rho^{k+1}} \left[\frac{3}{2} \Phi(u_i^k) - \frac{1}{2} \Phi(u_i^{k-1}) \right], \tag{4.8}$$

where the term Φ includes both convective and diffusive contributions:

$$\Phi(u_i^k) = -\rho^k u_j^k \frac{\partial u_i^k}{\partial x_j} + \frac{\partial \tau_{ij}^k}{\partial x_j}. \tag{4.9}$$

Once the intermediate velocity is computed, the pressure gradient is used to correct it and enforce mass conservation, yielding the final velocity:

$$u_i^{k+1} = u_i^* - \frac{\Delta t}{\rho^{k+1}} \frac{\partial p_1^{k+1}}{\partial x_i}. \tag{4.10}$$

At this point, the pressure field p^{k+1} remains unknown. Its evaluation is guided by the continuity equation, given in Eq. (3.12), which provides the necessary constraint to ensure that the corrected velocity field is mass-conserving. Taking the divergence of Eq. (4.10) and introducing the continuity equation (u_i^{k+1} is mass-conserving), a constant coefficient Poisson equation for hydrodynamic pressure can be obtained,

$$\nabla^2 p_1 = \frac{1}{\Delta t} \left[\left(\frac{\partial \rho}{\partial t} \right)^{k+1} + \nabla \cdot (\rho \mathbf{u})^* \right]. \tag{4.11}$$

The formulation and numerical treatment of the Poisson equation have been the subject of much research. Two strategies have emerged to address this problem: one is to solve a constant coefficient Poisson equation, and the other is to solve a variable coefficient formulation.

Chorin (1968) [38] was the first to introduce the projection method for incompressible flows, decoupling the updates of pressure and velocity to simplify the Navier–Stokes equations. Building on Chorin's projection method, McMurthry et al. (1986) [39] and Cook and Riley (1996) [40], in the context of reacting mixing flows, extended projection-based approaches to variable-density flows by incorporating variable-coefficient Poisson equations for pressure correction. They addressed the challenge of density variations by solving Eq. (4.11), where the density time derivative is approximated by a second-order explicit scheme,

$$\left(\frac{\partial \rho}{\partial t} \right)^{k+1} = \frac{3\rho^{k+1} - 4\rho^k + \rho^{k-1}}{2\Delta t}. \tag{4.12}$$

This second-order treatment for the time derivative of the density was found to be more stable than third-order explicit approximations, as discussed in their work. However, Nicoud (2000) [41]

pointed out that this approach can still introduce errors in energy conservation for inviscid flows because it does not fully enforce the divergence-free condition in the inviscid limit.

Lessani and Papalexandris (2006) [42] adopted a different strategy. They developed a predictor–corrector scheme for low Mach number variable-density flows where a second-order approximation for $\partial\rho/\partial t$ was implemented while solving a constant coefficient Poisson equation. This choice was possible because they simulated cases where the density change was smooth enough within a time step so that a second-order backward difference formula could capture the main effects without using a more complex variable-coefficient formulation. The advantage of this simplification is that constant coefficient Poisson solvers are computationally much cheaper compared to variable coefficient solvers. However, since the purpose of this work is to develop an algorithm that is applicable to a wider range of scenarios, including those with sharp density gradients, such an approximation for $\partial\rho/\partial t$ is not suitable.

An alternative approach to determine the hydrodynamic pressure field involves using Eq. (3.17), which is obtained by applying the continuity and energy equations to constrain the divergence of the velocity field. If we take the divergence of Eq. (4.10) again, a variable coefficient Poisson equation can also be obtained

$$\frac{\partial}{\partial x_i}\left(\frac{1}{\rho^{k+1}}\frac{\partial p_1^{k+1}}{\partial x_i}\right) = \frac{1}{\Delta t}\frac{\partial u_i^*}{\partial x_i} - \frac{1}{\Delta t}\frac{\partial u_i^{k+1}}{\partial x_i}, \tag{4.13}$$

where $\partial u_i^{n+1}/\partial x_i$ is substituted by Eq. (3.17), enforcing mass conservation in the system.

Dong and Shen (2012) [43], in the context of two-phase flows, proposed an approach that involves decomposing the variable density pressure gradient term into two parts: one with a constant coefficient and another that retains the variable coefficient

$$\frac{1}{\rho^{k+1}}\frac{\partial p_1^{k+1}}{\partial x_i} \rightarrow \frac{1}{\rho_*}\frac{\partial p_1^{k+1}}{\partial x_i} + \left(\frac{1}{\rho^{k+1}} - \frac{1}{\rho_*}\right)\frac{\partial p_1^*}{\partial x_i}, \tag{4.14}$$

where ρ_* represents a reference density that can be chosen based on the specific problem. In this work, the minimum density in the domain is adopted for stability purposes, following the approach of Dong and Shen (2012) [43]. The pressure p^* is an estimated pressure that is calculated by extrapolating from the previous two time steps. This extrapolated pressure must be adapted to different time integrations. For a Runge-Kutta time integration scheme (adopted in this work), the extrapolated pressure is

$$p_1^* = \left(1 + \sum_{l=1}^{k}\theta^l\frac{\Delta t^n}{\Delta t^{n-1}}\right)p_1^n - \sum_{l=1}^{k}\theta^l\frac{\Delta t^n}{\Delta t^{n-1}}p_1^{n-1}. \tag{4.15}$$

By substituting Eq. (4.14) into Eq. (4.13), a constant coefficient Poisson equation for pressure is obtained,

$$\frac{\partial^2 p_1^{k+1}}{\partial x_i^2} = \frac{\rho_*}{\Delta t}\frac{\partial u_i^*}{\partial x_i} - \frac{\rho_*}{\Delta t}\frac{\partial u_i^{k+1}}{\partial x_i} + \frac{\partial}{\partial x_i}\left[\left(1 - \frac{\rho_*}{\rho^{k+1}}\right)\frac{\partial p_1^*}{\partial x_i}\right]. \tag{4.16}$$

Dodd and Ferrante (2014) [44], in the same two-phase flow context, extended this technique and validated its performance for flows exhibiting large density and viscosity variations. This approach simplifies the variable-coefficient Poisson problem to a constant-coefficient one, improving computational efficiency.

This equation is solved using an FFT-based method implemented by Costa (2018) [33]. In this way, the hydrodynamic pressure is calculated and the corrected velocity field is computed by substituting Eq. (4.14) in Eq. (4.10),

$$u_i^{k+1} = u_i^* - \frac{\Delta t}{\rho_*}\frac{\partial p_1^{k+1}}{\partial x_i} - \Delta t\left(\frac{1}{\rho^{k+1}} - \frac{1}{\rho_*}\right)\frac{\partial p_1^*}{\partial x_i}. \tag{4.17}$$

This concludes the time advancement procedure for the current iteration, ensuring that both the thermodynamic and hydrodynamic fields evolve consistently with real-fluid behavior and satisfy the mass conservation constraint in a fully enclosed domain.

Demou et al. (2019) [45] adopted a similar pressure-splitting strategy in the context of natural convection in differentially heated cavities, characterized by strong temperature-induced density variations. This work considers the same setup, providing a relevant benchmark for evaluating the numerical treatment of temperature-induced density variations in real fluids.

4.2 Newton–Raphson iteration sensitivity to solver tolerance

An additional study was conducted to evaluate the sensitivity of the solver to the convergence tolerance. This analysis focuses on the performance of the Newton–Raphson algorithm used to update the thermodynamic pressure at each time step. All simulations in this section were carried out using sCO_2, with reference values of $T_{\text{ref}} = 669\,\text{K}$ and $P_{\text{ref}} = 16\,\text{MPa}$. Thermodynamic and transport properties were obtained from the CoolProp library and stored in a precomputed lookup table. The table covered the domain:

$$0.5\,T_{\text{ref}} \leq T \leq 1.5\,T_{\text{ref}}, \quad 0.5\,p_{\text{ref}} \leq p \leq 1.5\,p_{\text{ref}},$$

ensuring that the fluid remains entirely within the supercritical regime throughout the computational domain and the simulation time span.

Three solver tolerances were tested: 10^{-8}, 10^{-10} and 10^{-12}. For each configuration, the number of Newton–Raphson iterations required to reach convergence was recorded at each time step. The numerical analysis was performed for the differentially heated cavity configuration under two

imposed temperature ratios, $T_h/T_c = 1.5$ and 2.0, while the Rayleigh number was kept fixed at 10^{10}. To ensure this, the gravitational acceleration was adjusted accordingly for each case.

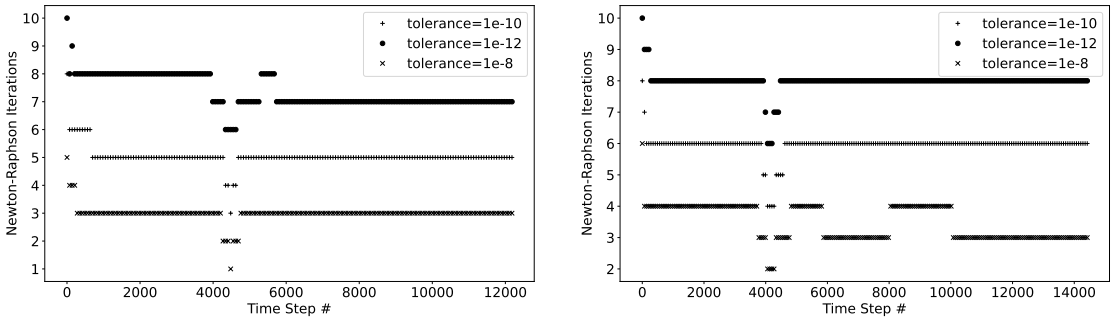

(a) $T_h/T_c = 1.5$ (b) $T_h/T_c = 2.0$

Figure 4.1: Time evolution of the first Newton–Raphson iterations for different solver tolerances using sCO_2.

As expected, a lower convergence tolerance results in a higher number of iterations in the Newton–Raphson method, since the solution must satisfy a stricter accuracy criterion.

It is also worth noting that, independently of the imposed tolerance, the number of Newton–Raphson iterations tends to converge to one as the flow approaches steady-state conditions. This indicates that thermodynamic pressure corrections become progressively smaller and the initial guess, taken from the previous time step, becomes sufficiently accurate to meet the convergence criterion. This behavior is illustrated in Figure 4.2 for a representative case with supercritical sCO_2, and for $T_h/T_c = 1.5$).

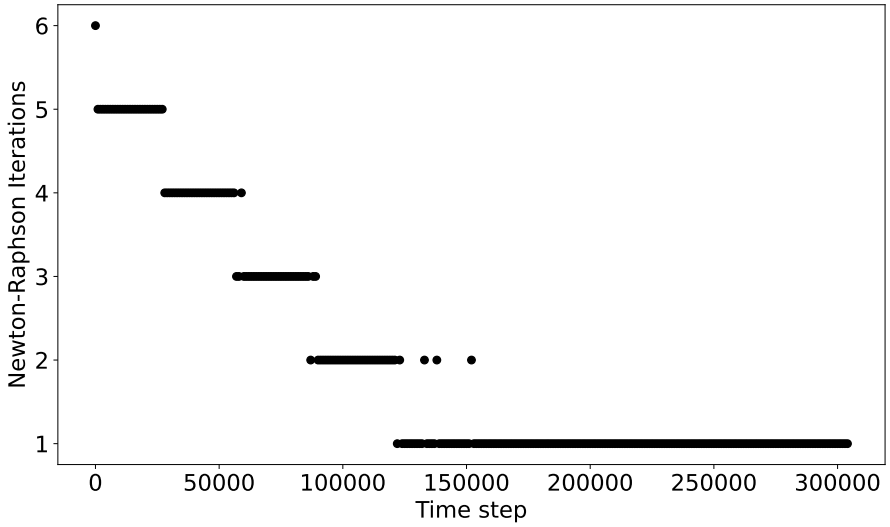

Figure 4.2: Time evolution of all Newton–Raphson iterations using sCO_2, showing the iteration count stabilizing at 1 as the flow reaches steady state.

Chapter 5

Validation

The numerical implementation developed in this work was evaluated using the differentially heated cavity (DHC), a classical benchmark for buoyancy-driven flows that has been extensively studied in the literature, including in the work of Le Quéré (1990) [46], which provides numerical reference solutions for natural convection in this configuration.

The DHC consists of a square enclosure with vertical walls at different temperatures, inducing buoyancy-driven flow under gravity. A schematic of the setup is shown in Figure 5.1.

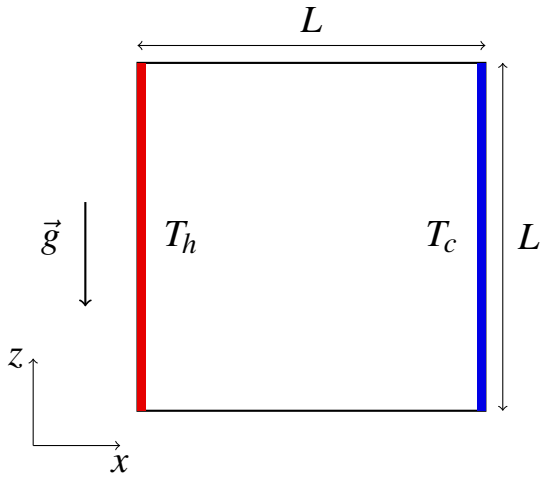

Figure 5.1: Schematic of the differentially heated cavity. The hot temperature T_h is imposed on the left wall and the cold temperature T_c on the right wall. Adiabatic conditions are applied on the top and bottom boundaries. No-slip velocity boundary conditions are imposed on all boundaries. Gravity acts downward along the z-axis.

In this configuration, the left wall is maintained at a hot temperature T_h and the right wall at a cold temperature T_c, with adiabatic conditions imposed at the top and bottom boundaries. Gravity acts downward along the z-axis. Simulations were performed for three temperature ratios, $T_h/T_c =$ 1.5, 2, and 3, covering different levels of density variation across the domain. In this study, the Rayleigh number, calculated as $Ra = (g\,\Delta\rho\,L^3)/(\mu\,\alpha)$, is based on the density difference between

the fluid adjacent to the hot and cold walls, rather than the temperature difference, following a non-Oberbeck–Boussinesq formulation. In this way, only the length of the cavity and gravity were adjusted to reach the same value for all cases. A value of $Ra = 2 \times 10^7$ was selected for all cases.

The comparison is made against the solver developed by Kottursheattar (2023) [34], which also uses the low Mach number approximation but assumes ideal-gas behavior. Density and transport properties are evaluated with Sutherland-type models:

$$\rho = \frac{P_0}{T}, \quad \lambda = T^{3/2}\frac{1+0.648}{T+0.648}, \quad \mu = T^{3/2}\frac{1+0.368}{T+0.368}. \tag{5.1}$$

Note that this temperature is nondimensional. To ensure a fair and consistent comparison, the present implementation did not rely on external libraries such as CoolProp for property evaluation. Instead, a precomputed property table was generated using the same Sutherland-type models and the ideal-gas assumption employed in Kottursheattar's solver [34]. Then, this table was used within the simulation to evaluate density, thermal conductivity, and dynamic viscosity as functions of temperature, enabling efficient and consistent property access throughout the numerical runs.

To assess the accuracy of the solver, the Nusselt number on the vertical walls, the temperature profile averaged along the vertical direction z as a function of the horizontal direction x, $\langle T \rangle_z(x)$, and the mean velocity components, namely the horizontal velocity averaged along x as a function of z, $\langle u \rangle_x(z)$, and the vertical velocity averaged along z as a function of x, $\langle w \rangle_z(x)$, were evaluated. The local Nusselt number on the wall was computed as

$$Nu = -\frac{L}{\Delta T}\left(\frac{\partial T}{\partial x}\right)_{\text{wall}}, \tag{5.2}$$

where L is the height of the cavity, $\Delta T = T_{\text{wall}} - T_{\text{ref}}$ is the temperature difference between the wall (hot or cold) and the reference temperature inside the cavity. This definition was applied to both the hot and the cold walls and was used consistently throughout all simulations in this work. Table 5.1 summarizes the comparison of the average Nusselt numbers on both hot and cold walls for three different imposed temperature ratios, under laminar and steady-state flow conditions.

Table 5.1: Comparison of average Nusselt number between the code by Kottursheattar (2023) and the present work for different temperature ratios.

Case	T_h/T_c	Nu_c	Nu_h	$(Nu_c + Nu_h)/2$	Relative error of mean Nu (%)
Present work	1.5	29.699	21.778	25.739	1.06
Kottursheattar (2023)		30.218	21.812	26.015	
Present work	2	43.758	24.000	33.879	1.09
Kottursheattar (2023)		43.903	24.604	34.254	
Present work	3	51.453	24.093	37.773	1.19
Kottursheattar (2023)		52.840	23.618	38.229	

The results show excellent agreement, with relative errors below 1.2% in all cases, confirming the accuracy of the present implementation in capturing heat transfer rates under varying buoyancy strengths. Since the Newton–Raphson method is applied to a linear equation of state like the ideal gas law, it effectively reduces to an analytical solution, and the pressure correction converges within a single iteration. Therefore, the small discrepancies observed are not due to the pressure solver but rather to the interpolation error introduced by the interpolation in the thermodynamic look-up table. Further validation was carried out by comparing the mean temperature and velocity profiles with the reference solution of Kottursheltar (2023) [34] as shown in Figure 5.2.

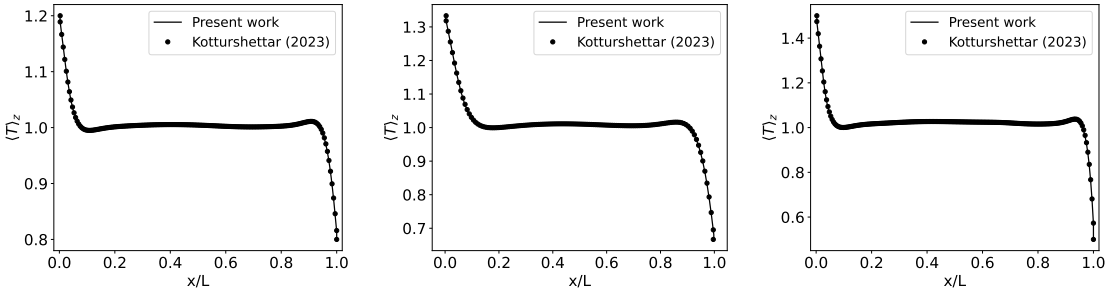

(a) Mean temperature vs x - $T_h/T_c = 1.5$ (b) Mean temperature vs x - $T_h/T_c = 2$ (c) Mean temperature vs x - $T_h/T_c = 3$

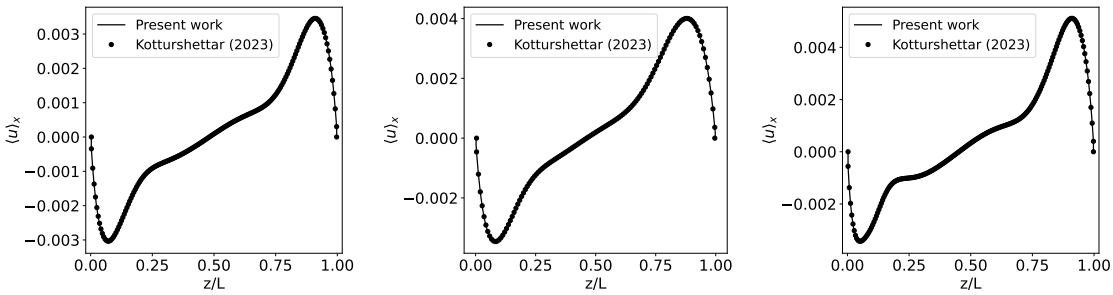

(d) Mean u velocity vs z - $T_h/T_c = 1.5$ (e) Mean u velocity vs z - $T_h/T_c = 2$ (f) Mean u velocity vs z - $T_h/T_c = 3$

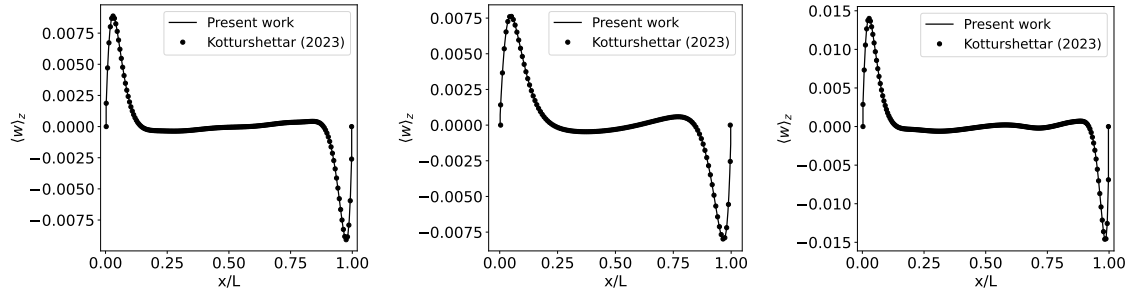

(g) Mean w velocity vs x - $T_h/T_c = 1.5$ (h) Mean w velocity vs x - $T_h/T_c = 2$ (i) Mean w velocity vs x - $T_h/T_c = 3$

Figure 5.2: Validation of DNS results obtained using the numerical method described in the present work (solid lines) against Kottursheltar (2023) (symbols) for cases with $T_h/T_c = 1.5$, 2, and 3.

The present results match closely with those from Kottursheattar (2023) [34] across all tested configurations ($T_h/T_c = 1.5$, 2 and 3). The profiles of mean temperature $\langle T \rangle_z(x)$, horizontal velocity $\langle u \rangle_z(z)$, and vertical velocity $\langle w \rangle_z(x)$ show consistent trends, correctly capturing the asymmetry and steep gradients induced by the imposed wall temperature ratio between the hot and cold sides.

As expected, the magnitude of the horizontal velocity increases as the temperature ratio increases from 1.5 to 3, indicating improved convective motion. Similarly, the vertical velocity also increases, reflecting the stronger circulation intensity. This behavior reflects the classical convection mechanism: as the fluid approaches the cold wall, it cools down, becomes denser, and descends. In contrast, near the hot wall, the fluid heats up, becomes less dense, and rises. This continuous cycle establishes a single large convection current with upward motion along the hot wall, horizontal transport across the top, downward motion along the cold wall, and return flow near the bottom boundary.

These cases for an ideal gas show how this fluid behaves for different temperature ratios imposed on the walls. All simulations fall within a regime where natural convection is well-developed while remaining steady. This makes these cases an excellent benchmark for the solver developed in this work, since no temporal averaging of the fields is required and the instantaneous profiles can be compared directly to reference data.

Together, these nine validation plots, along with the Nusselt number results, confirm that the numerical scheme accurately reproduces both the qualitative flow structures and the quantitative values of temperature and velocity fields for natural convection in a differentially heated cavity, in the ideal gas limit, and across different temperature ratios.

Chapter 6

Numerical Simulations

This chapter presents numerical simulations conducted in a differentially heated cavity for real fluids. The goal was to investigate how different substances, under realistic thermodynamic conditions, respond to imposed thermal gradients compared to the ideal gas case. A comparative study was carried out using three representative fluids: ideal gas, sCO_2, and pressurized liquid water across two different temperature ratios.

Although the main motivation of this work lies in the simulation of the flow of supercritical fluids, such as sCO_2, due to their practical relevance and complex thermodynamic behavior, the inclusion of pressurized liquid water demonstrates the versatility of the numerical algorithm in handling a wide variety of real fluids under single-phase conditions. Pressurized liquid water, in particular, was chosen to represent a dense and weakly compressible fluid, allowing a meaningful comparison with the thermally sensitive behavior of sCO_2 and the ideal gas. This contrast enables the identification of fundamental differences in heat transfer mechanisms under varying fluid compressibilities and property gradients.

6.1 Computational details

The DHC configuration, as discussed before, consists of a closed two-dimensional square cavity with vertical sidewalls maintained at different but constant temperatures: T_c (cold wall) and T_h (hot wall). The top and bottom boundaries are adiabatic, ensuring that heat transfer occurs only through natural convection driven by the difference in temperature between the vertical walls. The domain and boundary conditions follow well-established benchmarks in the literature, including the work of Le Quéré (1990) [46].

From a physical point of view, the differentially heated cavity represents a case of buoyancy-driven flow, where temperature gradients induce density variations that interact with gravity to produce natural convection (Davis (1983) [47]). The temperature difference between the vertical walls causes the warmer, lighter fluid near the hot wall to rise slightly, while the cooler, denser

fluid near the cold wall tends to sink, establishing a clockwise flow loop. These motions remain laminar and confined, with thermal and velocity boundary layers developing close to the vertical walls. In the central region of the cavity, thermal stratification dominates because of the relatively minor role of advection.

This configuration offers a simple yet insightful setup for investigating buoyancy-driven flows, making it particularly suitable for highlighting the differences between real fluids and the ideal gas.

6.2 Simulation cases

To systematically investigate the role of fluid properties under varying imposed wall temperatures, simulations were performed for three representative fluids: an ideal gas, sCO_2, and pressurized liquid water. The ideal gas case serves as a baseline, allowing the effects of real-fluid behavior to be clearly distinguished.

Each of these fluids was simulated in two temperature ratios, $T_h/T_c = 1.5$ and $T_h/T_c = 2$. These values were chosen so that sCO_2 remains sufficiently close to the critical region, where thermodynamic properties vary the most, so that pressurized liquid water remains in the same physical state throughout the cavity, avoiding phase change and the need for a multiphase formulation. To allow a consistent comparison between fluids with different thermophysical behavior, the Rayleigh number was fixed at 2×10^7 for the lower temperature ratio, calculated as $Ra = (\Delta\rho L^3 g)/(\mu\alpha)$, using the difference in density imposed on the walls and the viscosity and thermal diffusivity calculated with reference temperature and pressure. This allowed all fluids to start from the same buoyancy-driven regime, ensuring that the comparison begins under dynamically similar conditions. For the higher temperature ratio, only the temperature ratio was increased, and the Rayleigh number naturally diverged among the fluids because of their distinct thermophysical properties. This choice was made intentionally to capture the real impact of how property variations influence the dynamics of these flows for the different real fluids simulated. The simulated cases are summarized in Table 6.1.

Table 6.1: Simulated cases for the DHC configuration. sCO_2 is modeled in the supercritical regime, water is kept pressurized to remain in the liquid state, and the ideal gas assumes constant properties.

Fluid	**Simulated Ratios (T_h/T_c)**	**State**
CO_2	1.5, 2	Supercritical
Ideal Gas	1.5, 2	Ideal (constant properties)
Water	1.5, 2	Pressurized liquid

In order to perform consistent comparisons across fluids and temperature ratios, the thermodynamic domains were constructed based on a reference normalization. Specifically, the reference temperature was chosen so that the nondimensional temperatures satisfy the imposed temperature ratio T_h/T_c, while the arithmetic mean of the hot and cold nondimensional temperatures is equal to unity:

$$\frac{T_h + T_c}{2} = 1. \tag{6.1}$$

This constraint allows the definition of a fixed reference temperature around which the thermodynamic behavior is analyzed. Similarly, the pressure field is normalized using a reference pressure. To construct the lookup table used during the simulations, the dimensional temperature and pressure grids were nondimensionalized with respect to the chosen T_{ref} and P_{ref}. All thermodynamic properties, such as density, viscosity, thermal conductivity, specific heat, thermal expansion coefficient, and compressibility, were also normalized using their respective values evaluated in the reference state $(T_{\text{ref}}, P_{\text{ref}})$.

Moreover, the limits of the simulated thermodynamic space were selected such that the domain associated with the lower temperature ratio ($T_h/T_c = 1.5$) is fully contained within the domain used for the higher temperature ratio ($T_h/T_c = 2$):

$$\text{Domain}_{1.5} \subseteq \text{Domain}_2.$$

Figure 6.1 shows the thermodynamic simulation domains for each fluid and temperature ratio. In all cases, the domains are defined in terms of temperature and pressure and reflect the range over which each simula tion was performed. The liquid water thermodynamic domains were carefully validated with CoolProp to ensure that the fluid remained entirely in the liquid phase, since the solver used in this study assumes a single-phase formulation and does not account for phase change phenomena. The reference states were defined as follows: for sCO_2, $T_{\text{ref}} = 669.1\,\text{K}$ and $P_{\text{ref}} = 16.23\,\text{MPa}$; for pressurized liquid water, $T_{\text{ref}} = 450\,\text{K}$ for $T_h/T_c = 1.5$ and $T_{\text{ref}} = 425\,\text{K}$ for $T_h/T_c = 2$, both with $P_{\text{ref}} = 20\,\text{MPa}$.

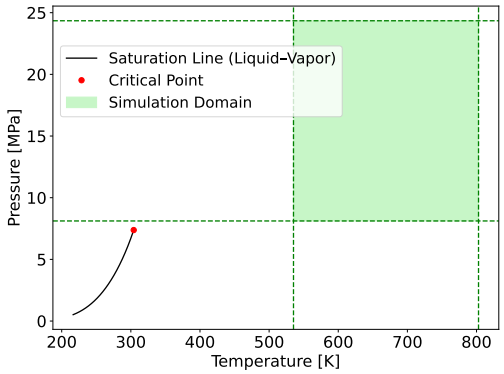

(a) sCO_2, $T_h/T_c = 1.5$

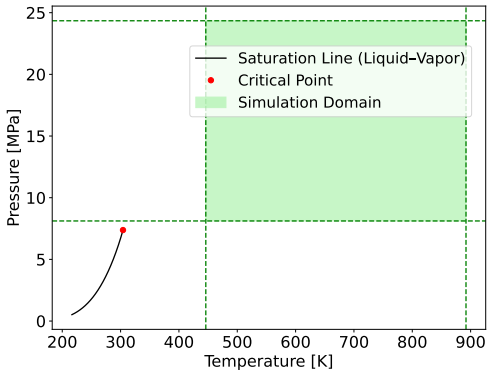

(b) sCO_2, $T_h/T_c = 2$

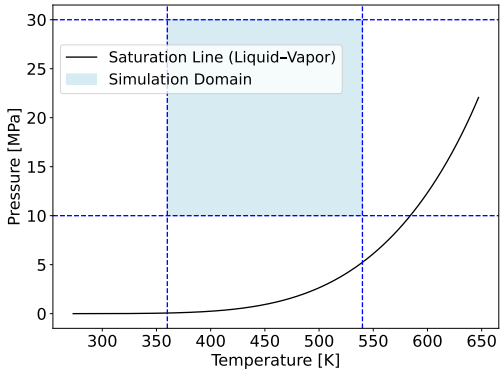

(c) Water, $T_h/T_c = 1.5$

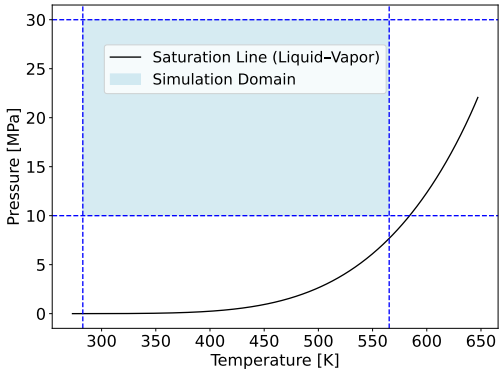

(d) Water, $T_h/T_c = 2$

Figure 6.1: Thermodynamic simulation domains for each tested fluid. Domains are defined in temperature-pressure space based on T_c and T_h boundaries. For sCO_2, the domains lie fully within the T_h/T_c ratios. Water was only simulated for the lower and higher temperature ratios where liquid-phase stability is guaranteed.

6.3 Transient evolution of the flow

In the present configuration, the flow is induced by a lateral temperature gradient between the hot and cold vertical walls. As the simulation evolves, thermal convection develops within the cavity, leading to the formation of a steady state.

To monitor the approach to this steady state, the Nusselt number on both the hot and cold walls was tracked over time. These values reflect the intensity of convective heat transfer and are expected to stabilize once a steady regime is established.

Figure 6.2 shows the temporal evolution of the Nusselt number on both vertical walls for the case with the temperature ratio $T_h/T_c = 1.5$. After an initial transient characterized by strong gradients and fluctuations, the Nusselt numbers on the hot and cold walls progressively converge

to stable values. This behavior is used as the primary criterion to confirm that a statistically steady state has been reached in each simulation.

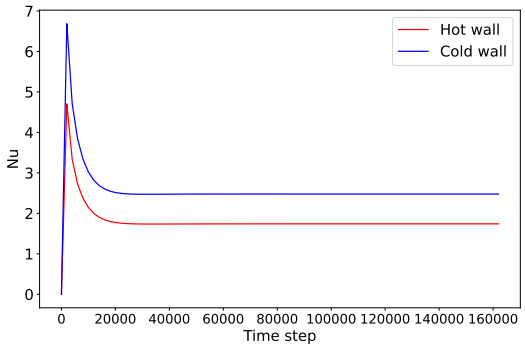

(a) sCO_2 - Nu at hot (red) and cold (blue) walls

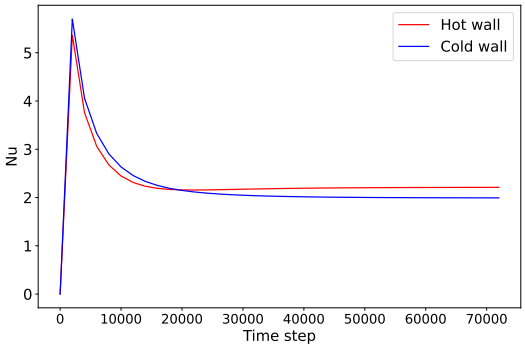

(b) Water - Nu at hot (red) and cold (blue) walls

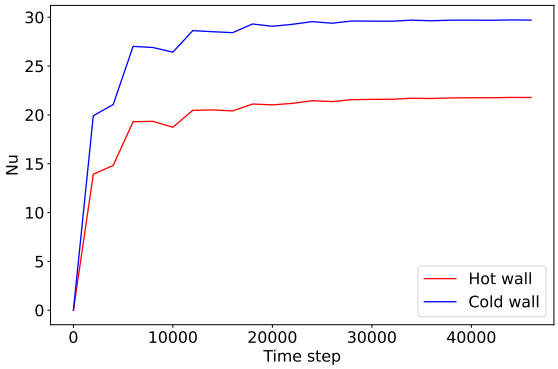

(c) Ideal Gas - Nu at hot (red) and cold (blue) walls

Figure 6.2: Time evolution of the height-averaged Nusselt number, Nu, at the hot and cold walls for each fluid in the case with temperature ratio $T_h/T_c = 1.5$. The stabilization of the curves confirms the attainment of statistically steady conditions.

It should be noted that the number of Newton–Raphson iterations required during the thermodynamic pressure update step varied significantly between fluids. In particular, pressurized liquid water required a noticeably higher number of iterations compared to sCO_2, especially during the early stages of the transient regime. This difficulty arises from the nearly incompressible nature of water, as its equation of state yields an extremely weak dependence of density on pressure. As a result, pressure corrections have minimal impact on the density field, making it harder for the Newton–Raphson method to converge efficiently. However, as discussed in Chapter 4, the iteration count progressively decreased and tended to stabilize at a single iteration per time step as the flow approached steady state.

6.4 Thermodynamic table and interpolation accuracy

All simulations presented in this work are based on a table of thermodynamic properties computed *a priori* using CoolProp, which covers a domain of temperature and pressure. This table is used to evaluate the properties of the fluid via third-order polynomial Lagrange interpolation during runtime (as discussed in Chapter 4).

To validate the accuracy of the interpolation procedure, a systematic error analysis was performed. For the two fluids studied, sCO_2 and pressurized liquid water, property tables were generated with increasing resolutions ranging from 50×50 to 550×550, covering the thermodynamic domains associated with the configurations $T_h/T_c = 1.5$ and $T_h/T_c = 2$. The interpolation error was calculated by evaluating the interpolated values at random (T, p) points within the domain and comparing them with the exact property values returned by CoolProp, which serves as a reference. The relative error was then calculated for each point and property.

Figure 6.3 shows the maximum and mean relative interpolation error for six key thermodynamic properties: density (ρ), dynamic viscosity (μ), specific heat at constant pressure (C_p), thermal expansion coefficient (β), isothermal compressibility (κ_T) and $\gamma = C_p/C_v$. The results confirm that the interpolation accuracy increases with resolution.

The interpolation error decreases consistently with increasing table resolution for all of the thermodynamic properties considered. Both the mean and maximum relative errors remain well below acceptable thresholds at higher resolutions. Specifically, a resolution of 400×400 ensures mean and maximum interpolation errors much lower than 0.01%, making it a reliable and efficient choice for the generation of property tables used in simulations.

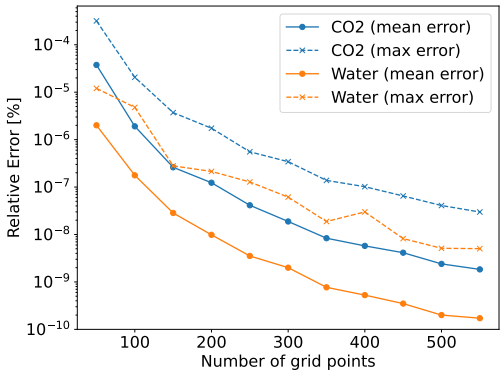

(a) Density (ρ)

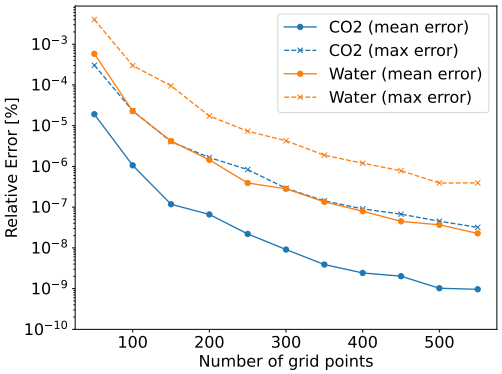

(b) Viscosity (μ)

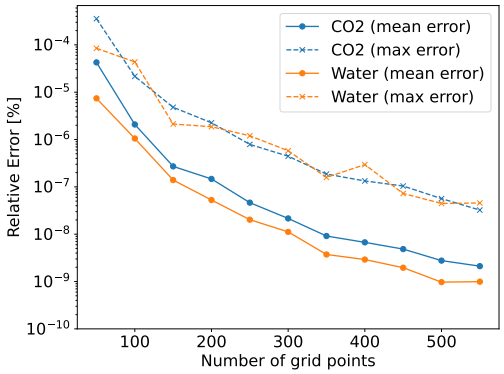

(c) Specific heat (C_p)

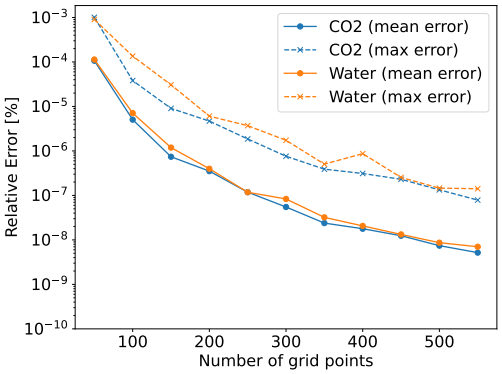

(d) Expansion coefficient (β)

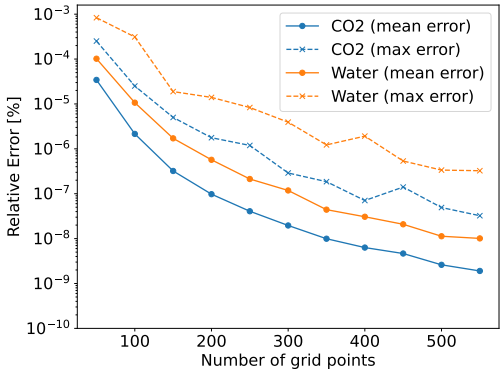

(e) Isothermal compressibility (κ_T)

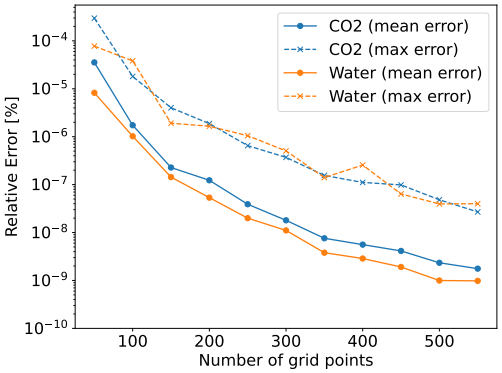

(f) $\gamma = C_p/C_v$

Figure 6.3: Mean and maximum relative interpolation errors for CO_2 and liquid water across different table resolutions, for six properties: density, viscosity, specific heat, expansion coefficient, compressibility, and γ.

Chapter 7

Results and Discussion

This chapter presents the results of the numerical simulations performed for the differentially heated cavity configuration using the real fluid models presented in Chapter 6. The aim is to analyze how the real thermophysical properties influence buoyancy-driven flow and heat transfer, in comparison to a substance that behaves as an ideal gas.

Two real fluids were considered: sCO_2, representative of a gas-like regime with strong property gradients near the critical point, and pressurized liquid water, which behaves as a dense, weakly compressible liquid. For each fluid, simulations were performed at two imposed temperature ratios, $T_h/T_c = 1.5$ and 2, allowing the evaluation of how the temperature differences between the hot and cold walls affect flow structure and energy transport.

The chapter begins with a grid convergence analysis to verify that the numerical results are independent of the mesh resolution. This is followed by a detailed examination of the temperature and velocity fields for both fluids with emphasis on how thermodynamic behavior influences the development of the flow. The Nusselt number is then analyzed to assess heat transfer between the different cases at both hot and cold walls. All results are interpreted in the context of classical natural convection theory, with particular attention to deviations arising from real-fluid effects in comparison to the ideal gas baseline.

7.1 Grid convergence analysis

To ensure the numerical accuracy and grid independence of the results, a grid convergence study was carried out for each working fluid and for each imposed temperature ratio. Three grid resolutions were considered: coarse, medium, and fine. For each case, the heat transfer behavior was evaluated on the basis of the Nusselt number on the hot and cold vertical walls.

The postprocessing phase included the application of the Richardson extrapolation method to estimate both the observed order of convergence and the asymptotic solution (grid independent),

as recommended by the American Society of Mechanical Engineers (1993) [48]. This approach assumes that the numerical result R varies with grid spacing η according to a power-law relationship:

$$R(\eta) = R_{\text{ext}} + C\eta^r, \tag{7.1}$$

where $R(\eta)$ represents the calculated result for a given mesh spacing, R_{ext} is the extrapolated value as the mesh is refined ($\eta \to 0$), C is a constant and r is the apparent order of convergence.

Using results R_1, R_2 and R_3 obtained from three progressively refined meshes with spacings η_1, η_2 and η_3, the order of convergence is calculated by:

$$r = \frac{\log\left(\dfrac{R_2 - R_1}{R_3 - R_2}\right)}{\log\left(\dfrac{\eta_1}{\eta_2}\right)}. \tag{7.2}$$

The extrapolated value is given by:

$$R_{\text{ext}} = R_3 + \frac{R_3 - R_2}{\left(\dfrac{\eta_2}{\eta_3}\right)^r - 1}. \tag{7.3}$$

Once R_{ext} is known, the relative error for each mesh is evaluated as:

$$\varepsilon_{\text{rel}} = \left|\frac{R_i - R_{\text{ext}}}{R_{\text{ext}}}\right| \times 100\%. \tag{7.4}$$

R was chosen to be the average of the Nusselt number on the cold and hot walls:

$$R = \frac{Nu_{\text{c}} + Nu_{\text{h}}}{2}. \tag{7.5}$$

Table 7.1 compiles the results for all test cases, presenting the Nusselt numbers and their corresponding relative errors. The final row of each configuration, labeled R.E., reports the Richardson-extrapolated value R_{ext}. Grid convergence was achieved for all cases, with relative errors below 1% on the finest grids, confirming that mesh-independent solutions were reached.

Table 7.1: Grid convergence results for sCO_2 and water at selected temperature ratios. R.E. stands for Richardson Extrapolation.

Fluid	T_h/T_c	Grid	Nu_c	Nu_h	$(Nu_c + Nu_h)/2$	Relative Error (%)
sCO_2	1.5	100×100	2.489	1.759	2.124	0.71
		150×150	2.484	1.747	2.116	0.31
		200×200	2.479	1.742	2.111	0.07
		R.E.	–	–	2.109	–
	2	100×100	2.915	1.650	2.283	1.93
		150×150	2.888	1.624	2.256	0.75
		200×200	2.877	1.617	2.247	0.35
		R.E.	–	–	2.239	–
water	1.5	100×100	2.006	2.218	2.112	0.57
		150×150	1.999	2.213	2.106	0.28
		200×200	1.996	2.208	2.102	0.09
		R.E.	–	–	2.100	–
	2	100×100	2.247	2.494	2.371	0.59
		150×150	2.239	2.486	2.363	0.25
		200×200	2.238	2.481	2.360	0.13
		R.E.	–	–	2.357	–

7.2 Physical interpretation

Following the grid convergence validation, the analysis now turns to the physical interpretation of the results for each fluid and temperature ratio. Table 7.2 shows the Rayleigh numbers for each simulation.

To gain insight into the physical behavior of the convective flow under different fluid properties, Figure 7.1 presents the dimensionless temperature and velocity magnitude fields for the three working fluids under the same imposed temperature ratio of $T_h/T_c = 1.5$. The temperature fields (left column of each row) exhibit clear differences in the strength of convection, which can be attributed to the increasing fluid density from ideal gas to sCO_2 and, furthermore, to pressurized liquid water. As the density of the fluid increases, the motion of the fluid becomes more restrained, making it harder for the buoyancy-driven flow to develop. This leads to weaker convection and temperature fields that are increasingly dominated by conduction.

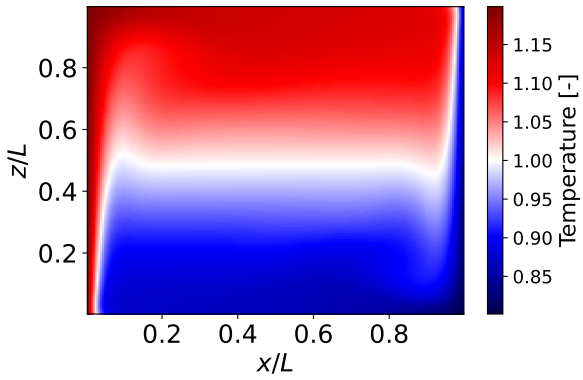

(a) Temperature – ideal gas

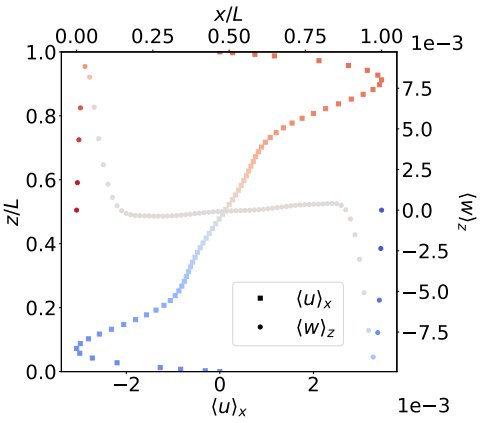

(b) Velocity – ideal gas

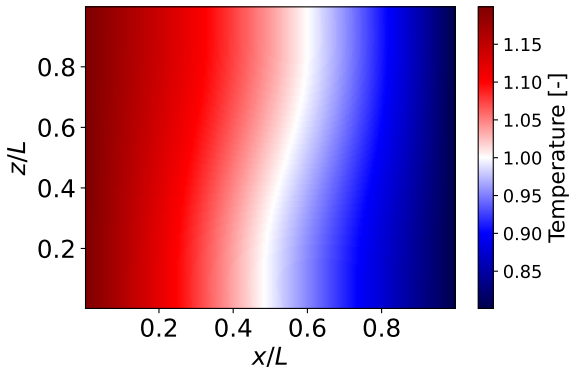

(c) Temperature – supercritical sCO_2

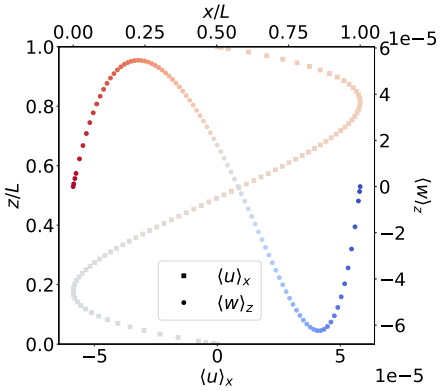

(d) Velocity – supercritical sCO_2

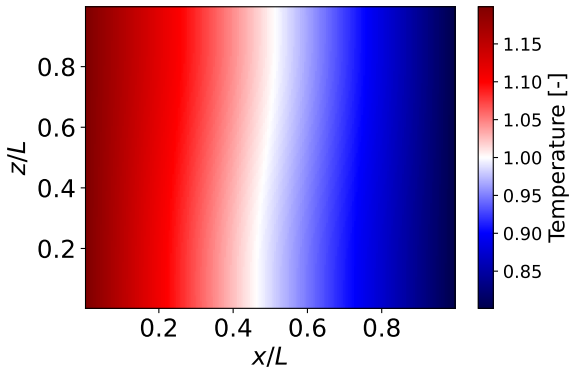

(e) Temperature – pressurized liquid water

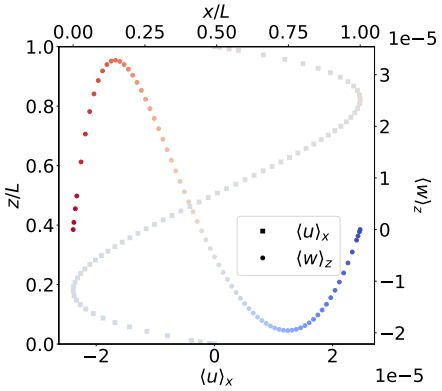

(f) Velocity – pressurized liquid water

Figure 7.1: Comparison of dimensionless temperature fields and velocity magnitude contours for $T_h/T_c = 1.5$, across ideal gas, supercritical sCO_2 and pressurized liquid water.

Table 7.2: Rayleigh numbers for different fluids and temperature ratios.

Temperature Ratio	Ideal Gas	sCO_2	Pressurized Water
1.5	2×10^7	2×10^7	2×10^7
2	4.62×10^7	3.75×10^7	1.56×10^8

These observations are further corroborated by the velocity magnitude contours (right column of each row in Figure 7.1), where the flow intensity and circulation strength decrease progressively from the ideal gas to sCO_2 and to liquid water. The magnitudes of the two components of velocity, $\langle u \rangle_x$ and $\langle w \rangle_z$, drop from the order of $10^{-3}\,\mathrm{m/s}$ in the ideal gas case to $10^{-5}\,\mathrm{m/s}$ for real fluids, with liquid water exhibiting the lowest values within that range. Fluid inertia, constrained by higher density, limits the development of typical circulatory patterns of convective flows.

To further investigate how the intensification of the imposed wall temperatures affects the flow behavior of different fluids, Figure 7.2 presents the dimensionless temperature and velocity magnitude fields for the same three working fluids, now under $T_h/T_c = 2$. The increase in the temperature ratio accentuates the contrasts between the behaviors of the fluids, particularly in terms of thermal stratification and flow circulation.

As the temperature ratio increases from $T_h/T_c = 1.5$ to $T_h/T_c = 2$, a general intensification of natural convection is observed in all fluids. This is consistent with classical buoyancy-driven behavior, where stronger temperature gradients lead to larger density differences, and thus increase the driving force for circulation. The isotherms become more distorted, and the velocity fields show greater recirculation and kinetic energy. For $T_h/T_c = 2$, the two velocity components increase in all cases; however, the ideal gas continues to exhibit significantly stronger motion, with velocity magnitudes on the order of $10^{-3}\,\mathrm{m/s}$, compared to $10^{-4}\,\mathrm{m/s}$ for the real fluids.

Although the Rayleigh numbers used in this study would typically be considered high for ideal gas (yet still in the steady regime, as shown by Le Quéré (1990) [46]), the effective strength of convection varies significantly compared to the case of fluids. For dense real fluids, such as sCO_2 and pressurized liquid water, the higher inertia associated with their higher densities - $\rho_{sCO_2} = 128.35\,\mathrm{kg/m^3}$ and $\rho_{H_2O} = 925.19\,\mathrm{kg/m^3}$ - limits the development of buoyancy-driven motion, leading to heat transfer regimes closer to conduction. In contrast, the ideal gas, with a much lower reference density of $\rho_{IG} = 1.184\,\mathrm{kg/m^3}$, exhibits more vigorous convective behavior, making conduction comparatively less dominant. This occurs despite the fact that the Rayleigh number of the ideal gas is lower than that of pressurized water for $T_h/T_c = 2$, as shown in Table 7.2. The enhanced convection in the ideal gas case arises from its significantly lower viscosity and density, which reduce viscous resistance and inertia, thus facilitating more dynamic flow responses to buoyancy forces. Therefore, comparing Rayleigh numbers across fluids with drastically different

thermophysical properties must be interpreted with caution, as the same *Ra* may correspond to different flow intensities depending on the fluid's diffusivities and inertial effects.

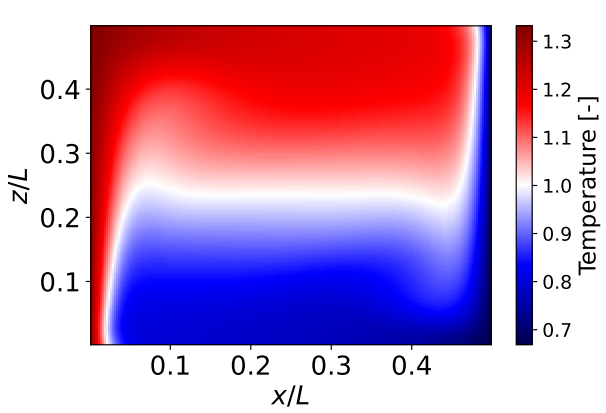

(a) Temperature – ideal gas

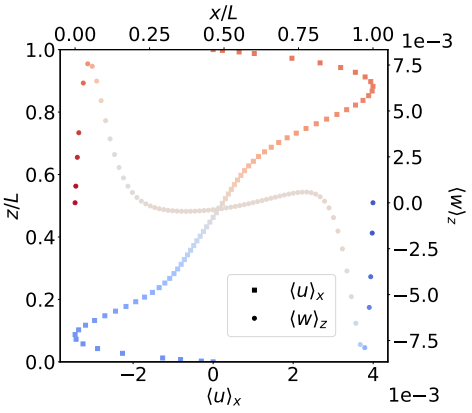

(b) Velocity – ideal gas

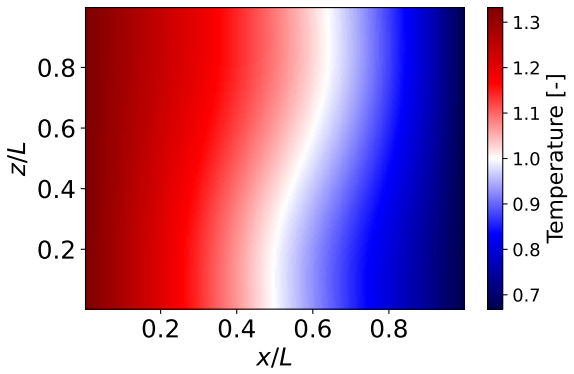

(c) Temperature – supercritical sCO_2

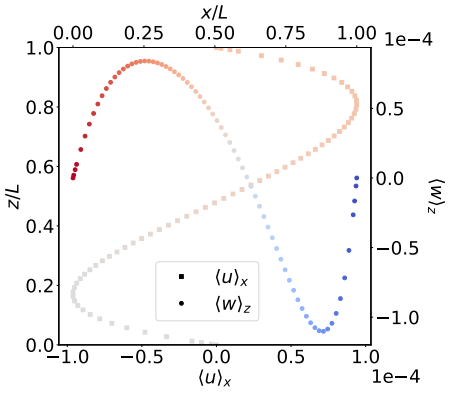

(d) Velocity – supercritical sCO_2

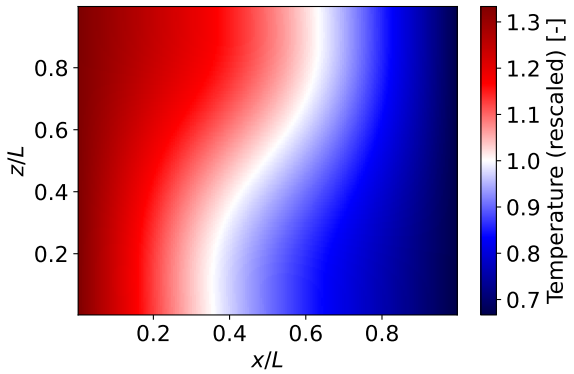

(e) Temperature – pressurized liquid water

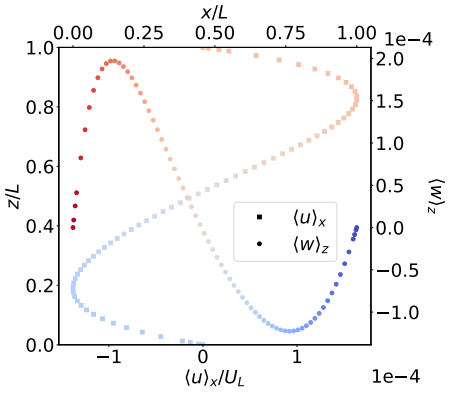

(f) Velocity – pressurized liquid water

Figure 7.2: Comparison of dimensionless temperature fields and velocity magnitude contours for $T_h/T_c = 2$, across ideal gas, supercritical sCO_2 and pressurized liquid water.

An interesting inversion in convective behavior is observed when comparing sCO_2 with pressurized liquid water. In the lower temperature ratio ($T_h/T_c = 1.5$), sCO_2 exhibits stronger convective activity across the cavity due to its lower density. However, this trend reverses at $T_h/T_c = 2$, as liquid water exhibits a significantly larger density variation with temperature throughout the domain. This pronounced gradient improves the buoyancy forces sufficiently to overcome the fluid's higher inertia, resulting in more vigorous convective motion than in sCO_2. In contrast, the density of sCO_2 changes more gradually within the same range, limiting the enhancement of buoyant forces.

To clarify this behavior, Figure 7.3 shows the density profiles with temperature at the reference pressure for each fluid. These profiles reveal that, although liquid water remains consistently denser than sCO_2, it experiences a greater absolute change in density over the same temperature range. This greater density variation increases driving buoyancy forces, helping explain why water exhibits a stronger convective motion at $T_h/T_c = 2$, exceeding that of sCO_2. In contrast, the more limited density variation of sCO_2 restricts its buoyancy-driven enhancement under the same imposed wall temperatures.

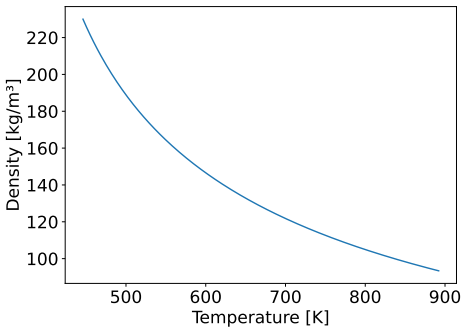

(a) Supercritical sCO_2

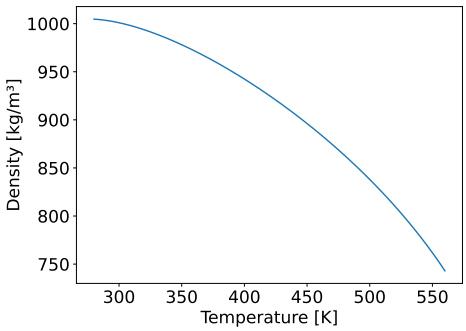

(b) Pressurized liquid water

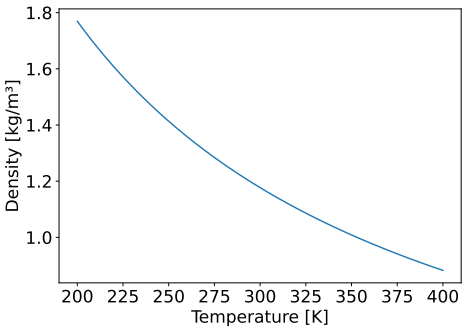

(c) Ideal gas

Figure 7.3: Density as a function of temperature at reference pressure for the three working fluids.

These differences are quantitatively reflected in the calculated Rayleigh numbers (Table 7.2). For $T_h/T_c = 2$, the Rayleigh number for water exceeds that of sCO_2, indicating a stronger thermally driven instability. This shift shows the importance of evaluating flow behavior in terms of real-flow property variation. It also confirms that, under sufficiently high thermal gradients and pressures, dense liquids such as pressurized water can shift from a conduction-dominated regime to one where convective heat transfer becomes predominant, exceeding gas-like fluids in overall convective heat transfer.

To quantify the differences in heat transfer across fluids and imposed temperature ratios, Figure 7.4 compiles the Nusselt numbers obtained for each case on both hot and cold walls. The ideal gas exhibits the highest convective heat transfer rate, particularly at the higher temperature ratio. This is primarily due to its higher thermal diffusivity, as previously defined, which allows the fluid to adjust rapidly to the imposed wall temperatures. This promotes the formation of significant temperature differences that enhance buoyancy forces, leading to convective transport that is clearly dominant over conduction. Note the different vertical scales used in the two subplots, reflecting the much higher Nusselt numbers achieved by the ideal gas compared to the real fluids.

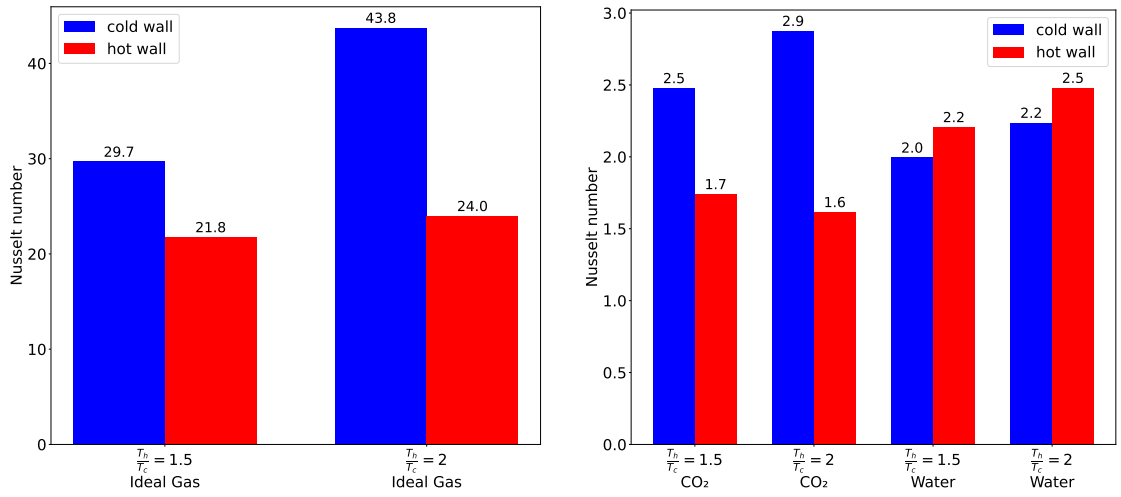

(a) Ideal gas

(b) Real fluids

Figure 7.4: Average Nusselt number on the hot and cold walls for different fluids and temperature ratios.

As the imposed temperature ratio increases from $T_h/T_c = 1.5$ to 2, a consistent intensification of convective transport is observed in all working fluids. This is reflected in the growth of the local Nusselt numbers at both the hot and cold walls, a trend directly attributable to the stronger buoyancy forcing arising from the higher density gradients. The thermal and velocity fields, previously discussed, confirm this behavior: increased distortion of isotherms and intensified recirculating flow structures point to a more vigorous convective regime at higher temperature ratios.

Among the fluids studied, the ideal gas displays the highest Nusselt numbers. This outcome is expected given its significantly lower density and higher thermal diffusivity, which together promote stronger convective motion. The ideal gas responds more vigorously to the imposed thermal gradients, as evidenced by the sharp temperature variations and strong circulation patterns visible in the flow field of Figures 7.1 and 7.2. The high Nusselt values are therefore a direct consequence of enhanced mixing and thermal transport, a behavior not matched by the real fluids under the same conditions because of lower thermal diffusion values.

More subtle but equally important are the differences observed between sCO_2 and pressurized liquid water in terms of the Nusselt number. Both are modeled with full thermodynamic realism, and their behavior under imposed wall temperatures diverges significantly. sCO_2 consistently exhibits a Nusselt number profile characterized by $Nu_c > Nu_h$. This asymmetry is typical of gas-like systems, where thermal conductivity increases with temperature, causing the hotter wall to conduct better than the colder wall. Since the Nusselt number can be defined as the ratio of the total heat transfer to conductive heat transfer, and since this number is calculated over the entire wall (taking into account the local Nusselt number distribution) in steady state, one can state that the numerator of this number must be equal at both hot and cold walls because of energy conservation. Consequently, a higher thermal conductivity near the hotter wall leads to a smaller Nusselt number compared to that at the cold wall. A similar trend is observed in the ideal gas case, which, being fundamentally a gas-like fluid, exhibits the same asymmetry in the Nusselt number between the two walls.

In contrast, pressurized liquid water shows the opposite behavior. The Nusselt numbers for water show a clear inversion, with $Nu_h > Nu_c$. In this case, thermal conductivity decreases with increasing temperature, making the colder wall more effective at conducting heat than the hotter wall. As a result, for the same total heat transfer, a lower thermal conductivity near the hot wall leads to a higher Nusselt number at the hot wall. This trend reflects the typical behavior of liquid-like fluids, where thermophysical properties vary differently with temperature compared to gas-like systems.

These differences in how gas-like and liquid-like fluids transfer heat can be further observed in the velocity profiles of Figures 7.1 and 7.2 for sCO_2 and pressurized liquid water. In the case of sCO_2, the vertical profile $\langle w \rangle_z$ is clearly shifted towards the cold wall in terms of magnitude, the peak on the colder side being greater in absolute value than on the hotter side. This indicates a stronger buoyancy-driven motion near the cold wall. This behavior is consistent with the asymmetry in thermal conductivity, which enhances the thermal gradients on the cold side and promotes more vigorous convective flow in that region.

In contrast, pressurized liquid water exhibits the opposite trend in its vertical velocity profile $\langle w \rangle_z$. The peak magnitude is higher near the hot wall, indicating that the buoyancy-driven motion

is more intense on that side. This behavior is aligned with the decrease in thermal conductivity with temperature, which sharpens the thermal gradient near the hot wall and enhances the local buoyant acceleration. As a result, the convective motion becomes stronger near the hot boundary.

Chapter 8

Conclusions and Future Work

This work addressed a critical gap in the scientific literature concerning the simulation of closed systems with real-fluid behavior under low Mach number approximation. Although low Mach number formulations are well-established for open systems and ideal gas (both open and closed systems), their application to fully enclosed domains involving real fluids remains limited. To overcome this, a new solver was developed to simulate thermally driven flows of real fluids in closed domains, where the thermodynamic pressure evolves in time to ensure mass conservation.

The numerical implementation was based on a low Mach number formulation and incorporated a Newton–Raphson procedure to iteratively compute the thermodynamic pressure at each time step. The thermodynamic pressure of the previous time level was used as the initial estimate for the Newton-Raphson iteration, enabling stable and efficient convergence. Thermodynamic properties were evaluated using real fluid equations of state with the CoolProp library, and third-order polynomial Lagrange interpolation was applied to a precomputed property table to reduce computational cost.

An important advantage of the developed solver is its ability to simulate real fluid dynamics at significantly lower computational cost compared to solving the fully compressible Navier–Stokes equations. By filtering out acoustic effects while retaining the essential thermodynamic couplings, the low Mach number framework enables faster simulations without sacrificing physical accuracy, making it highly suitable for long-time integrations and parameter studies in closed systems.

The solver was validated against ideal-gas results for $T_h/T_c = 1.5$, $T_h/T_c = 2$ and $T_h/T_c = 3$, showing excellent agreement in the limit of ideal gas. Then it was applied to simulate the differentially heated cavity configuration, considering two temperature ratios, $T_h/T_c = 1.5$ and $T_h/T_c = 2$, with a Rayleigh number fixed on the order of 10^7 for the lower temperature ratio. Three fluids were studied: an ideal gas, sCO_2 (supercritical carbon dioxide), and pressurized liquid water.

The results demonstrated that the solver not only accurately recovers the expected behavior in the ideal gas limit, validating its formulation, but also produces physically consistent results for

real fluids such as sCO_2 and pressurized liquid water. These results align with an established understanding of thermally driven flows in such regimes. Specifically, for increasing temperature ratios, the solver correctly captured the intensification of convective transport. Although denser fluids generally exhibit lower buoyant accelerations for a given temperature difference, in real fluids, the presence of larger density differences between both hot and cold walls can overcome this effect, promoting stronger convective circulation. A key observation was the distinction in the thermal transport behavior: ideal gas and sCO_2, which behave in a gas-like manner with relatively high thermal diffusivity, exhibited higher Nusselt numbers on the cold wall, while pressurized liquid water showed the opposite trend, with greater heat transfer occurring on the hot wall. This inversion is consistent with the thermodynamic variation of thermal conductivity and density across the cavity, further supporting the physical reliability of the solver under real gas conditions.

Overall, the developed solver successfully extends low Mach number formulations to closed systems with real-fluid thermodynamics, offering a robust tool to study supercritical convection and energy transport in complex regimes.

Future work

The present study opens several directions for further research:

- **Verification against real-fluid benchmark cases:** Although the solver was validated using ideal gas conditions, further verification with benchmark DNS or experimental results for real fluids is essential to confirm accuracy under realistic conditions.
- **Extension to higher Rayleigh numbers:** Future studies should investigate regimes with significantly higher Rayleigh numbers to assess the onset and evolution of convective instabilities. This would enable a more comprehensive comparison between the real-fluid and ideal-gas behaviors in fully turbulent convection.
- **Data-driven turbulence modeling in the supercritical regime:** Now that a solver capable of handling closed systems with real fluid behavior has been developed, a promising research direction would be training machine learning models to predict Reynolds stresses in supercritical regimes under low Mach conditions. By leveraging high-fidelity DNS data generated with the current solver, it would be possible to develop data-driven turbulence closures specifically tailored for strongly non-linear thermodynamic conditions, contributing to the advancement of turbulence modeling for real fluids.
- **Development of heat transfer correlations for supercritical regimes:** The validated solver enables the generation of reliable datasets under realistic thermodynamic conditions. This opens the possibility of deriving new heat transfer correlations specifically tailored to supercritical fluids in closed systems, where existing models based on ideal gas or subcritical

assumptions may fail. These correlations could significantly support engineering design and system optimization in high-efficiency thermal systems using real fluids.

- **Extension to multiphase formulations:** An important future direction involves extending the current methodology to handle multiphase flows, including phase change phenomena. This would allow the solver to capture phase change behaviors such as condensation, boiling, or near-critical pseudo-boiling for closed systems with real fluid properties.

The numerical framework developed in this thesis provides a solid foundation for simulating real-fluid flows in closed systems, laying the groundwork for future studies of supercritical fluid dynamics and their application in more advanced thermal systems.

Bibliography

[1] M. J. Moran, H. N. Shapiro, D. D. Boettner, and M. B. Bailey. *Fundamentals of Engineering Thermodynamics*. John Wiley & Sons, Hoboken, New Jersey, U.S., 2010.

[2] O. A. Marzouk. Subcritical and supercritical Rankine steam cycles under elevated temperatures up to 900°C and absolute pressures up to 400 bara. *Advances in Mechanical Engineering*, 16:1–18, 2024. doi: 10.1177/16878132231221065.

[3] B. S. Petukhov. Heat transfer in a single-phase medium under supercritical conditions (Heat transfer in single phase medium at near critical state parameters). *High Temperature*, 6: 696–709, 1968.

[4] W. B. Hall, J. D. Jackson, and A. Watson. A review of forced convection heat transfer to fluids at supercritical pressures. In *Proceedings of the institution of mechanical engineers, conference proceedings*, volume 182, pages 10–22. SAGE Publications Sage UK: London, England, 1967.

[5] K. Yamagata, K. Nishikawa, S. Hasegawa, T. Fujii, and S. Yoshida. Forced convective heat transfer to supercritical water flowing in tubes. *International Journal of Heat and Mass Transfer*, 15:2575–2593, 1972. doi: 10.1016/0017-9310(72)90148-2.

[6] J. W. Ackerman. Pseudoboiling heat transfer to supercritical pressure water in smooth and ribbed tubes. *ASME Journal of Heat and Mass Transfer*, 92:490–497, 1970. doi: 10.1115/1.3449698.

[7] V. A. Kurganov and A. G. Kaptilnyi. Flow structure and turbulent transport of a supercritical pressure fluid in a vertical heated tube under the conditions of mixed convection. Experimental data. *International Journal of Heat and Mass Transfer*, 36:3383–3392, 1993. doi: 10.1016/0017-9310(93)90020-7.

[8] I. L. Pioro and R. B. Duffey. Experimental heat transfer in supercritical water flowing inside channels (survey). *Nuclear Engineering and Design*, 235:2407–2430, 2005. doi: 10.1016/j.nucengdes.2005.05.034.

[9] T. Xiong, X. Yan, Z. Xiao, Y. Li, Y. Huang, and J. Yu. Experimental study on flow instability in parallel channels with supercritical water. *Annals of Nuclear Energy*, 48:60–67, 2012. doi: 10.1016/j.anucene.2012.05.018.

[10] Y. Li, G. Xin, B. Yuan, S. Zhang, and W. Du. Experimental investigation on natural circulation heat transfer of supercritical CO_2 in a closed loop. *International Journal of Heat and Mass Transfer*, 200:123503, 2023. doi: 10.1016/j.ijheatmasstransfer.2022.123503.

[11] S. Koshizuka, N. Takano, and Y. Oka. Numerical analysis of deterioration phenomena in heat transfer to supercritical water. *International Journal of Heat and Mass Transfer*, 38: 3077–3084, 1995. doi: 10.1016/0017-9310(95)00008-W.

[12] E. Laurien. Development of numerical wall-functions to model the heat transfer of supercritical fluids. In *Proceedings of the 2010 International Congress on Advances in Nuclear Power Plants-ICAPP'10*, page 27–38. American Nuclear Society, 2010.

[13] Q. L. Wen and H. Y. Gu. Numerical simulation of heat transfer deterioration phenomenon in supercritical water through vertical tube. *Annals of Nuclear Energy*, 37:1272–1280, 2010. doi: 10.1016/j.anucene.2010.05.022.

[14] W. S. Kim, S. He, and J. D. Jackson. Assessment by comparison with DNS data of turbulence models used in simulations of mixed convection. *International journal of heat and mass transfer*, 51:1293–1312, 2008. doi: 10.1016/j.ijheatmasstransfer.2007.12.002.

[15] P. Jiang, Y. Zhang, and R. Shi. Experimental and numerical investigation of convection heat transfer of CO_2 at super-critical pressures in a vertical mini tube. In *International Conference on Nanochannels, Microchannels, and Minichannels*, volume 47608, pages 583–590, 2006. doi: 10.1115/ICNMM2006-96110.

[16] J. H. Bae, J. Y. Yoo, and H. Choi. Direct numerical simulation of turbulent supercritical flows with heat transfer. *Physics of Fluids*, 17(10), 2005. doi: 10.1063/1.2047588.

[17] M. V. Morkovin. Effects of compressibility on turbulent flows. *Mécanique de la Turbulence*, 367:26, 1962.

[18] G. N. Coleman, J. Kim, and R. D. Moser. A numerical study of turbulent supersonic isothermal-wall channel flow. *Journal of Fluid Mechanics*, 305:159–183, 1995. doi: 10.1017/S0022112095004587.

[19] A. Majda and J. Sethian. The derivation and numerical solution of the equations for zero Mach number combustion. *Combustion Science and Technology*, 42:185–205, 1985. doi: 10.1080/00102208508960376.

[20] F. Battista, F. Picano, and C. M. Casciola. Turbulent mixing of a slightly supercritical van der Waals fluid at low-mach number. *Physics of Fluids*, 26, 2014. doi: 10.1063/1.4873200.

[21] F. Creta, R. Lamioni, P. E. Lapenna, and G. Troiani. Interplay of Darrieus-Landau instability and weak turbulence in premixed flame propagation. *Physical Review E*, 94:053102, 2016. doi: 10.1103/PhysRevE.94.053102.

[22] P. E. Lapenna and F. Creta. Mixing under transcritical conditions: An a-priori study using direct numerical simulation. *The Journal of Supercritical Fluids*, 128:263–278, 2017. doi: 10.1016/j.supflu.2017.05.005.

[23] P. E. Lapenna, R. Lamioni, P. P. Ciottoli, and F. Creta. Low-Mach number simulations of transcritical flows. In *2018 AIAA Aerospace Sciences Meeting*, page 0346, 2018. doi: 10.2514/6.2018-0346.

[24] W. Wang, S. He, C. Moulinec, and D. R. Emerson. Direct numerical simulation of thermal stratification of supercritical water in a horizontal channel. *Computers & Fluids*, 261:105911, 2023. doi: 10.1016/j.compfluid.2023.105911.

[25] J. W. R. Peeters. *Turbulence and turbulent heat transfer at supercritical pressure*. PhD thesis, TU Delft, Mekelweg 5, 2628 CD Delft, nov 2016.

[26] H. Nemati. *Direct numerical simulation of turbulent heat transfer to fluids at supercritical pressures*. PhD thesis, TU Delft, Mekelweg 5, 2628 CD Delft, nov 2016.

[27] R. Span and W. Wagner. Equations of state for technical applications. II. Results for non-polar fluids. *International Journal of Thermophysics*, 24:41–109, 2003. doi: 10.1023/A:1022310214958.

[28] R. Span and W. Wagner. A new equation of state for carbon dioxide covering the fluid region from the triple-point temperature to 1100 K at pressures up to 800 MPa. *Journal of Physical and Chemical Reference Data*, 25:1509–1596, 1996. doi: 10.1063/1.555991.

[29] I. H. Bell, J. Wronski, S. Quoilin, and V. Lemort. Pure and Pseudo-pure Fluid Thermophysical Property Evaluation and the Open-source Thermophysical Property Library CoolProp. *Industrial & Engineering Chemistry Research*, 53:2498–2508, 2014. doi: 10.1021/ie4033999.

[30] E. W. Lemmon, I. H. Bell, M. L. Huber, and M. O. McLinden. NIST Standard Reference Database 23: Reference Fluid Thermodynamic and Transport Properties-REFPROP, Version 10.0, National Institute of Standards and Technology, 2018. URL https://www.nist.gov/srd/refprop.

[31] T. Poinsot and D. Veynante. *Theoretical and numerical combustion*. RT Edwards, Inc., P.O. Box 27388, Philadelphia, Pennsylvania 19118, US, 2005.

[32] D. R. Gaskell. *Introduction to the Thermodynamics of Materials*. Taylor & Francis, New York, 2008.

[33] P. Costa. A FFT-based finite-difference solver for massively-parallel direct numerical simulations of turbulent flows. *Computers & Mathematics with Applications*, 76:1853–1862, 2018. doi: 10.1016/j.camwa.2018.07.034.

[34] S. Kotturshettar. Low-Mach-number solver for stratified channel flows with ideal gas. Technical report, Mekelweg 5, 2628 CD Delft, jul 2023.

[35] G. S. Jiang and C. W. Shu. Efficient implementation of weighted ENO schemes. *Journal of Computational Physics*, 126:202–228, 1996. doi: 10.1006/jcph.1996.0130.

[36] C. A. Kennedy, M. H. Carpenter, and R. M. Lewis. Low-storage, explicit Runge-Kutta schemes for the compressible Navier-Stokes equations. *Applied Numerical Mathematics*, 35:177–219, 2000. doi: 10.1016/S0168-9274(99)00141-5.

[37] E. Rinaldi. *Models and simulation of non-ideal fluid flows in unconventional turbomachinery*. PhD thesis, TU Delft, Mekelweg 5, 2628 CD Delft, oct 2015.

[38] A. J. Chorin. Numerical solution of the Navier-Stokes equations. *Mathematics of Computation*, 22:745–762, 1968. doi: 10.1090/S0025-5718-1968-0242392-2.

[39] P. A. McMurtry, W. H. Jou, J. Riley, and R. W. Metcalfe. Direct numerical simulations of a reacting mixing layer with chemical heat release. *AIAA journal*, 24:962–970, 1986. doi: 10.2514/3.9371.

[40] A. W. Cook and J. J. Riley. Direct numerical simulation of a turbulent reactive plume on a parallel computer. *Journal of Computational Physics*, 129:263–283, 1996. doi: 10.1006/jcph.1996.0249.

[41] F. C. Nicoud. Numerical study of a channel flow with variable properties. Technical report, Center for Turbulence Research, 481 Panama Mall, Stanford, CA 94305, EUA, jan 1998.

[42] B. Lessani and M. V. Papalexandris. Time-accurate calculation of variable density flows with strong temperature gradients and combustion. *Journal of Computational Physics*, 212:218–246, 2006. doi: 10.1016/j.jcp.2005.07.001.

[43] S. Dong and J. Shen. A time-stepping scheme involving constant coefficient matrices for phase-field simulations of two-phase incompressible flows with large density ratios. *Journal of Computational Physics*, 231:5788–5804, 2012. doi: 10.1016/j.jcp.2012.04.041.

[44] M. S. Dodd and A. Ferrante. A fast pressure-correction method for incompressible two-fluid flows. *Journal of Computational Physics*, 273:416–434, 2014. doi: 10.1016/j.jcp.2014.05.024.

[45] A. D. Demou, C. Frantzis, and D. G. E. Grigoriadis. A low-Mach methodology for efficient direct numerical simulations of variable property thermally driven flows. *International Journal of Heat and Mass Transfer*, 132:539–549, 2019. doi: 10.1016/j.ijheatmasstransfer.2018.12.018.

[46] P. Le Quéré. Accurate solutions to the square thermally driven cavity at high Rayleigh number. *Computers & Fluids*, 20:29–41, 1991. doi: 10.1016/0045-7930(91)90025-D.

[47] G. Davis. Natural convection of air in a square cavity: a benchmark numerical solution. *International Journal for Numerical Methods in Fluids*, 3:249–264, 1983. doi: 10.1002/fld.1650030305.

[48] American Society of Mechanical Engineers. Fluids Engineering Division. *Quantification of uncertainty in computational fluid dynamics*. American Society of Mechanical Engineers, New York, 1993.

Appendix A

Derivation of dimensional low Mach approximation

The unsteady flow of a non-reacting, single-species fluid is described by the fully compressible Navier–Stokes equations. The governing system of equations comprises the continuity and momentum equations, the sensible enthalpy (or energy) transport equation, and a general equation of state that couples thermodynamic variables (Poinsot and Veynante (2005) [31]):

$$\frac{\partial \rho}{\partial t} + \frac{\partial}{\partial x_i}(\rho u_i) = 0, \tag{A.1a}$$

$$\frac{\partial}{\partial t}(\rho u_j) + \frac{\partial}{\partial x_i}(\rho u_i u_j) = -\frac{\partial p}{\partial x_j} + \frac{\partial \tau_{ij}}{\partial x_i} + \rho f_i, \tag{A.1b}$$

$$\frac{\partial \rho h_t}{\partial t} + \frac{\partial}{\partial x_i}(\rho u_i h_t) = \frac{\partial p}{\partial t} - \frac{\partial}{\partial x_i}\left(\lambda \frac{\partial T}{\partial x_i}\right) + \frac{\partial}{\partial x_j}(\tau_{ij} u_i), \tag{A.1c}$$

$$\mathscr{F}(\rho, T, p) = 0. \tag{A.1d}$$

Before proceeding with nondimensionalization, it is worth recalling that the low-Mach number approximation is appropriate for flows where acoustic waves are not dynamically significant. In such regimes, pressure adjusts instantaneously across the domain, and the flow remains close to local thermodynamic equilibrium. This is common in natural convection, slow combustion, and many low-speed aerothermal flows.

To nondimensionalize the governing equations, characteristic reference scales are introduced. The spatial and temporal coordinates are scaled by a characteristic length L_0 and velocity u_0, respectively. For enthalpy, $h_0 = a^2$ is selected, where a is the reference speed of sound. This choice is motivated by the low Mach number framework, which assumes $M = u/a \ll 1$, implying that kinetic energy is negligible compared to internal energy. Accordingly, the reference pressure is defined as $p_0 = \rho_0 a^2$, consistent with the dynamic pressure scaling. These choices ensure proper

balancing of inertial, pressure, and thermal terms in the nondimensionalized equations (see Majda and Sethian (1985) [19]).

$$\begin{aligned} \tilde{x} &= \frac{x}{L}, \quad \tilde{t} = \frac{tu_0}{L}, \quad \tilde{u_i} = \frac{u_i}{u_0}, \quad \tilde{\rho} = \frac{\rho}{\rho_0}, \quad \tilde{T} = \frac{T}{T_0}, \\ \tilde{p} &= \frac{p}{\rho_0 a_0^2}, \quad \tilde{\mu} = \frac{\mu}{\mu_0}, \quad \tilde{\lambda} = \frac{\lambda}{\lambda_0}, \quad \tilde{h}_t = \frac{h_t}{a_0^2}, \quad \tilde{f}_j = \frac{f_j L}{u_0^2}. \end{aligned} \tag{A.2}$$

Mass conservation equation

Nondimensionalizing the continuity equation and dividing through by the reference scale $\rho_0 u_0/L_0$, the nondimensional form is obtained:

$$\frac{\partial \tilde{\rho}}{\partial \tilde{t}} + \frac{\partial}{\partial \tilde{x}_i}(\tilde{\rho}\tilde{u}_i) = 0 \tag{A.3}$$

This expression preserves the structure of the original equation and remains valid for both compressible and low Mach number regimes.

Momentum conservation equation

Similarly, by nondimensionalizing the variables in the momentum equation and dividing through by $\rho_0 u_0^2/L_0$, the equation becomes:

$$\tilde{\rho}\left(\frac{\partial \tilde{u}_j}{\partial \tilde{t}} + \tilde{u}_i \frac{\partial \tilde{u}_j}{\partial \tilde{x}_i}\right) = -\frac{1}{M^2}\frac{\partial \tilde{p}}{\partial \tilde{x}_j} + \frac{1}{Re}\frac{\partial \tilde{\tau}_{ij}}{\partial \tilde{x}_i} \tag{A.4}$$

Here, $M = u_0/a$ denotes the reference Mach number and $Re = \rho_0 u_0 L_0/\mu_0$ is the Reynolds number.

Energy conservation equation

Applying the nondimensional variables to the energy equation and, again, dividing through by the characteristic scale $\rho_0 h_0 u_0/L_0$, yields:

$$\tilde{\rho}\frac{D\tilde{h}_t}{D\tilde{t}} = \frac{\partial \tilde{p}}{\partial \tilde{t}} - \frac{1}{Pe}\frac{\partial}{\partial \tilde{x}_i}\left(\tilde{\lambda}\frac{\partial \tilde{T}}{\partial \tilde{x}_i}\right) + \frac{M^2}{Re}\frac{\partial}{\partial \tilde{x}_j}(\tilde{\tau}_{ij}\tilde{u}_i) \tag{A.5}$$

Here is introduced the reference Peclé number, $Pe = \rho_0 c_p u_0 L_0/\lambda_0$. Since the Mach number in this regime is small ($M << 1$), the kinetic energy contribution in the total enthalpy becomes negligible compared to the sensible enthalpy. Thus, the dimensionless total enthalpy can be approximated by the sensible enthalpy alone ($h_t \approx h_s$). To simplify the notation, h_s will be written as h and all variables are assumed to be nondimensional, so the tilde symbol ($\sim$) is omitted henceforth.

For real fluids, the sensible enthalpy depends on both temperature and pressure. Using total differentials, it can be written as:

$$dh = \left(\frac{\partial h}{\partial T}\right)_p dT + \left(\frac{\partial h}{\partial p}\right)_T dp \tag{A.6}$$

In the case of ideal gas, the specific enthalpy depends solely on temperature, since $(\partial h/\partial p)_T = 0$. However, for real fluids, this partial derivative becomes non-negligible, reflecting how pressure influences molecular interactions and thus internal energy storage.

The total differential of enthalpy thus captures both thermal and mechanical contributions to energy changes. This dependence plays a key role in energy transport and must be retained in low Mach number formulations involving real fluids, where ignoring the pressure derivative could lead to significant errors in heat transfer predictions.

Applying the chain rule, the temporal and spatial derivatives of enthalpy become:

$$\frac{\partial h}{\partial t} = \left(\frac{\partial h}{\partial T}\right)_p \frac{\partial T}{\partial t} + \left(\frac{\partial h}{\partial p}\right)_T \frac{\partial p}{\partial t} \tag{A.7}$$

$$\frac{\partial h}{\partial x_i} = \left(\frac{\partial h}{\partial T}\right)_p \frac{\partial T}{\partial x_i} + \left(\frac{\partial h}{\partial p}\right)_T \frac{\partial p}{\partial x_i} \tag{A.8}$$

Substituting these expressions into the energy equation yields:

$$\rho\left[\left(\frac{\partial h}{\partial T}\right)_p \frac{\partial T}{\partial t} + \left(\frac{\partial h}{\partial p}\right)_T \frac{\partial p}{\partial t} + u_j\left(\left(\frac{\partial h}{\partial T}\right)_p \frac{\partial T}{\partial x_j} + \left(\frac{\partial h}{\partial p}\right)_T \frac{\partial p}{\partial x_j}\right)\right] = \frac{\partial p}{\partial t} - \frac{1}{Pe}\frac{\partial q_j}{\partial x_j} \tag{A.9}$$

Recalling that $\left(\frac{\partial h}{\partial T}\right)_p = C_p$ and $\left(\frac{\partial h}{\partial p}\right)_T = V - T\left(\frac{\partial V}{\partial T}\right)_p$, and introducing the thermal expansion coefficient $\beta = \frac{1}{V}\left(\frac{\partial V}{\partial T}\right)_p$, this expression simplifies to

$$\left(\frac{\partial h}{\partial p}\right)_T = V(1-\beta T), \tag{A.10}$$

which will be used in the enthalpy decomposition to account for real-fluid behavior.

The energy equation thus becomes:

$$\rho\left[C_p\frac{\partial T}{\partial t} + u_j\left(C_p\frac{\partial T}{\partial x_j} + V(1-\beta T)\frac{\partial p}{\partial x_j}\right)\right] = \beta\ T\ \frac{\partial p}{\partial t} - \frac{1}{Pe}\frac{\partial}{\partial x_i}\left(\frac{\partial q_i}{\partial x_i}\right) \tag{A.11}$$

Low Mach number formulation

To derive the governing equations in the zero-Mach-number limit, note that terms proportional to M^2 in the nondimensionalized equations vanish. Following the approach in Majda and Sethian (1985) [19], the primary variables are expanded - density, velocity, pressure, and temperature - in asymptotic series with respect to powers of M^2, i.e., around a reference state corresponding to $M \to 0$:

$$\rho = \rho^{(0)} + M^2\rho^{(1)} + M^4\rho^{(2)} + \cdots, \tag{A.12a}$$

$$u_i = u_i^{(0)} + M^2 u_i^{(1)} + M^4 u_i^{(2)} + \cdots, \tag{A.12b}$$

$$p = p^{(0)} + M^2 p^{(1)} + M^4 p^{(2)} + \cdots, \tag{A.12c}$$

$$T = T^{(0)} + M^2 T^{(1)} + M^4 T^{(2)} + \cdots. \tag{A.12d}$$

Other thermophysical quantities, such as viscosity μ, thermal conductivity λ, specific heat at constant pressure c_p, and thermal expansion coefficient β, are evaluated consistently from the state variables p and T, and thus reduce to their leading-order counterparts as $M^2 \to 0$: for example, $\lambda(p,T) \to \lambda^{(0)}(p^{(0)},T^{(0)})$. Substituting these expansions into the nondimensional equations and collecting terms by order of magnitude in M, we obtain the leading-order system:

$$\mathscr{O}(1): \quad \frac{D\rho^{(0)}}{Dt} = -\rho^{(0)}\frac{\partial u_j^{(0)}}{\partial x_j}, \tag{A.13a}$$

$$\mathscr{O}(M^{-2}): \quad \frac{\partial p^{(0)}}{\partial x_i} = 0, \tag{A.13b}$$

$$\mathscr{O}(1): \quad \rho^{(0)}\frac{Du_i^{(0)}}{Dt} = -\frac{\partial p^{(1)}}{\partial x_i} + \frac{\partial \tau_{ij}^{(0)}}{\partial x_j}, \tag{A.13c}$$

$$\mathscr{O}(1): \quad \rho^{(0)}C_p^{(0)}\frac{DT^{(0)}}{Dt} = \beta^{(0)}T^{(0)}\frac{dp^{(0)}}{dt} - \frac{\partial}{\partial x_j}\left(\lambda\frac{\partial T^{(0)}}{\partial x_j}\right), \tag{A.13d}$$

$$\mathscr{O}(1): \quad \mathscr{F}(p^{(0)},\rho^{(0)},T^{(0)}) = 0. \tag{A.13e}$$

Because Eq. (A.13b) implies that the leading-order pressure is spatially uniform, the momentum equation at this order does not determine the flow field. Therefore, to close the system, the next-order momentum balance (Eq. A.13c) must be retained. Note also that the final form of the equations is presented in dimensional form.

From a numerical standpoint, the low Mach formulation decouples the fast acoustic time scales from the convective and diffusive dynamics, allowing for significantly larger time steps in time-dependent simulations.